Reviewed Preprint
v1 • February 26, 2026
Not revised

Reviewed Preprint
v2 • June 18, 2026
Revised by authors

Cribriform Plate Microenvironment Assembles a Suppressive Myeloid Network during EAE-induced Neuroinflammation

Collin Laaker[1], Martin Hsu[2], Andy Madrid[1], Jenna Port[3], Sophia M Vrba[3], Melinda Herbath[3], Cameron Baenen[3], Mohan Kumar[3], Thanthrige Thiunuwan Priyathilaka[3], Matyas Sandor[3,*], Zsuzsanna Fabry[3,*]

[1]Neuroscience Training Program, University of Wisconsin Madison, Madison, United States • [2]Department of Microbiology-Immunology, University of North Carolina at Chapel Hill, Chapel Hill, United States • [3]Department of Pathology and Laboratory Medicine, School of Medicine and Public Health, University of Wisconsin Madison, Madison, United States

For correspondence: zfabry@wisc.edu

* Co-senior authors

Competing interests: No competing interests declared

Funding: See page 23

Reviewing editor: Isaac M Chiu, Harvard Medical School, United States

eLife Assessment

This **important** study identifies the cribriform plate as a key neuroimmune interface that shapes myeloid cell responses during neuroinflammation. Using imaging, flow cytometry, and single-cell approaches in a mouse model of EAE, the authors provide **convincing** evidence that dendritic cells and macrophages accumulate in PDPN-rich niches and have transcriptional features consistent with tolerogenic or immunosuppressive states. The work is technically strong and novel, and future studies will be needed to define the functional consequences of these myeloid cell states in autoimmunity.

https://doi.org/10.7554/eLife.110460.2.sa3

Abstract

During neuroinflammation, CD11c+CD11b+ myeloid cells accumulate at the cribriform plate, a key cerebrospinal fluid (CSF) and antigen outflow site in mice. At this site, podoplanin (PDPN)-expressing cells, including lymphatic vessels and meningeal layers, expand to create a distinct drainage microenvironment. In this study we sought to characterize myeloid cells which populate this region using a mouse model of neuroinflammation, experimental autoimmune encephalomyelitis (EAE). Utilizing a combination of immunohistochemistry, flow cytometry, and scRNAseq, we report that macrophages and dendritic cells (DCs) from this region display unique expressional signatures related to tolerance, cell death, and reduced inflammatory profile. Together this data supports that myeloid retention at the cribriform plate and olfactory bulb meninges promotes a local immunosuppressive environment.

Introduction

Meningeal microenvironments are highly dynamic during neuroinflammatory disease, which is critical for the progression and resolution of inflammation in the central nervous system (CNS) (Rustenhoven et al., 2021; Hitpass Romero et al., 2025). For example, in the dura, the outermost meningeal layer, lymphatic vessels can adapt and respond to brain inflammation; sampling cerebrospinal fluid (CSF), waste, and CNS-antigens to help coordinate immunity during neuroinflammation (Zhang et al., 2025b; Louveau et al., 2018). Additionally, $CD11b^{+}CD11c^{+}$ peripheral myeloid populations rapidly infiltrate the brain and meningeal niches, accessing antigen, upregulating MHC-II, and migrating through this meningeal lymphatic network, underscoring their role in antigen presentation and T-cell activation during infection and autoimmunity in the central nervous system (CNS) (Jordão et al., 2019; Clarkson et al., 2015,

2017; Louveau et al., 2018). While there are increasing studies on the regulation of immune cells in the dorsal dural immune hubs (Rustenhoven et al., 2021; Fitzpatrick et al., 2024), there is still little knowledge of the phenotypes of myeloid cells that accumulate at CSF efflux sites along the base of the brain, like the cribriform plate lymphatics.

Recently, our lab and others have shown that Lyve-1$^+$ lymphatic vessels between the olfactory bulbs access CSF through gaps in the arachnoid layer along olfactory nerve bundles, enabling fluid, antigen, and immune cell drainage to the cervical lymph nodes (Hsu et al., 2019, 2022; Spera et al., 2023; Jin et al., 2025). This lymphatic niche at the cribriform plate expands during experimental autoimmune encephalomyelitis (EAE), a mouse model of Multiple Sclerosis (MS), and upregulates genes related to leukocyte cross-talk (adhesion, chemotaxis, antigen processing and presentation, and activation) (Hsu et al., 2022). Furthermore, we previously showed that a majority of the retained cells at the cribriform plate lymphatic niche during neuroinflammation were CD11c$^+$ CD11b$^+$ (Hsu et al., 2019, 2022), implicating myeloid subsets, including DCs, were the primary immune cells that are recruited, retained, and potentially regulated in the meningeal-lymphatic environment at the cribriform plate(Hsu et al., 2022).

In the context of brain inflammation, the regulation and efflux pathways of DCs from the CNS are still poorly understood (Laaker et al., 2023). Our lab and others have shown that during EAE, intracerebrally and intracisternally injected DCs can exit the intracranial space and drain to the cervical lymph nodes in a CCR7-dependent manner (Clarkson et al., 2017; Karman et al., 2004; Louveau et al., 2018). Interestingly, intracranially retained CCR7-KO DCs exacerbate autoimmune-mediated neuroinflammation, restimulating infiltrating autoreactive T-cells near brain tissue (Clarkson et al., 2017). While evidence supports that effluxing pro-inflammatory DCs from the intracranial space can further stimulate T-cell populations in the draining lymph nodes (Hsu et al., 2019), there is also data to support that DCs migrating in the olfactory bulb region of mice acquire a tolerogenic cell state (Mohammad et al., 2014). Thus, understanding how CD11b$^+$CD11c$^+$ cells interact at the cribriform plate could give important insight into how DC cell states are conditioned at CSF-efflux from the skull. Importantly, cranial nerve bundles, like the brain, are also surrounded by meningeal layers and interface with CSF to form a specialized perineural microenvironment (PME) as they extend from the CNS and traverse the skull (Fahmy et al., 2021; Proulx, 2021).

While peripheral nerve bundles are increasingly recognized as a unique neuroimmune niche that promote immunosuppressive tumor microenvironments (TME)(Baruch et al., 2025; Liebig et al., 2009; Chen et al., 2019) and tissue repair after injury through reprogramming of local and recruited myeloid cells(Ydens et al., 2020), the PME of cranial nerve bundles as they exit the skull during neuroinflammation is still poorly understood. Further complicating analysis, inflammatory environments in the meninges, including near the PME, often elevate extracellular matrix (ECM)-related tissue niches where immune cells, lymphatics, fibroblasts, and blood vessels are tightly interwoven in dense cell-cell interactions (Dorrier et al., 2022). Interestingly, during EAE we find increased podoplanin expression at the cribriform plate which is rich with myeloid cells. Understanding this cell-cell cross-talk could be essential to understanding how DCs and other myeloid cells contacting the meningeal-lymphatic environment are reprogrammed during disease.

In this study, we identified populations of CCR7$^+$ DCs within this microenvironment that had enriched pathways related to programmed cell death (PD-1), tolerance induction, and inhibited interferon-signaling pathways. Additionally, our scRNAseq dataset and IHC analysis support for a role of CCR2$^+$ monocytes and integration of alternatively activated Arginase-1 (*Arg1*) and CHI3L3 (*Chil3*) macrophages into a PDPN$^+$ microenvironment at the cribriform plate during EAE. We hypothesize that the cribriform plate functions as an immune interface between the CNS and the periphery, simultaneously accessing draining antigen and CSF while dynamically reshaping its perineural myeloid microenvironment to regulate the phenotype of DCs and antigen outflow to the cervical lymph nodes.

Results

CSF1R$^+$, CD11c$^+$, and MHC-II$^+$ cells are in cell-cell contact with an expanded PDPN$^+$ PME around olfactory nerve bundles during EAE

We previously identified that CD11b$^+$ CD11c$^+$ myeloid cells increase near olfactory nerves and along cribriform lymphatic vessels during EAE-induced inflammation (Hsu et al., 2022; Laaker et al., 2025). To more holistically understand the spatial environment of myeloid cells at the meningeal–lymphatic drainage regions of the cribriform plate (Figure 1A), we induced EAE in CSF1R-GFP mice and stained decalcified cribriform plate sections for the common lymphatic markers PDPN and LYVE-1 (Figure 1B). As reported previously (Hsu et al., 2019), LYVE-1$^+$ regions are primarily found in the spaces directly between the olfactory bulbs, running adjacent to outwardly projecting midline olfactory nerves above the cribriform plate (Figure 1B). Directly surrounding olfactory nerve bundles is a prominent PDPN$^+$LYVE-1^{neg} layer which links the perineural region to double positive PDPN$^+$LYVE-1$^+$ lymphatics (Figure 1B; **zoom panel**).

PDPN not only labels lymphatic vessels, but also efficiently labels meningeal layers surrounding them along the olfactory nerve layer, including fibroblasts and their associated extracellular matrix (ECM) (Hitpass Romero et al., 2025; Møllgård et al., 2023; Çavdar et al., 2024). To understand if this PDPN increases around the olfactory nerve layer and is associated with antigen presenting cells (APCs) during EAE, we costained for MHCII and PDPN. We found an elevated number of MHC-II$^+$ cells in PDPN regions, likely DCs, activated macrophages, and B cells (Figure 1C). CSF1R-GFP$^+$ myeloid cells were colocalized to PDPN$^+$ PME during EAE (Figure 1D), with perineural PDPN increasing in thickness during active EAE (Figure 1E). To better visualize CD11c$^+$ DCs, we analyzed sections from CD11c-eYFP mice during peak EAE disease severity, and observed similar relationships between DCs and perineural PDPN$^+$ regions (Figure 1F-H). While many CD11c$^+$ cells within the parenchyma of the OB are likely activated microglia (Figure 1G), large numbers of CD11c$^+$ cells were also observed in direct contact with perineural PDPN$^+$ at the cribriform plate (Figure 1H), and embedded into the ECM (Figure 1I-J). CD11c$^+$ cells in the olfactory bulb parenchyma display a ramified, microglia-like morphology consistent with tissue-resident or parenchymal surveillance cells, whereas those infiltrating the cribriform plate perineural niche show a rounded, non-ramified morphology more consistent with recently recruited monocyte-derived DCs or macrophages. Additionally, while PDPN labels the cribriform plate lymphatic vasculature, it also defines the meningeal-immune interface at the border of both the olfactory bulb and olfactory nerve bundles. Thus, the PDPN$^+$ PME harbors elevated numbers of myeloid cells that directly associate with the cribriform plate lymphatic vasculature and meningeal stroma.

Cribriform plate PME is embedded with ARG1 and CHI3L3 cells during neuroinflammation

Podoplanin ECM environments are commonly associated with immunosuppressive macrophages (Wang et al., 2022a; Swartz and Lund, 2012; Bieniasz-Krzywiec et al., 2019). To determine whether these alternatively activated macrophages accumulate *in situ* at the cribriform plate during EAE, we performed immunofluorescence staining on decalcified cribriform plate sections using the alternative activation markers CHI3L3 (*Chil3*) and ARG1 (*Arg1*), together with Lyve-1 and PDPN to delineate cribriform meningeal lymphatic structures. Here, we found CHI3L3$^+$ cells increased at the cribriform plate during EAE (Figure 2A-E), with many CHI3L3$^+$ cells adhering directly to the PDPN$^+$ PME regions (Figure 2B-C). Similarly, Arg1-expressing cells at the cribriform plate increased during EAE and were highly colocalized within perineural PDPN$^+$ (Figure 2F-H). However, as the size of PDPN regions increases, subsequently the regions which can hold ARG1+ and CHI3L3+ cells also increase making interpretation difficult. Together, our data suggests the accumulation of alternatively polarized macrophages in PDPN$^+$ PME regions during peak EAE disease severity (Murray, 2017; Jiang et al., 2014; Xin et al., 2025).

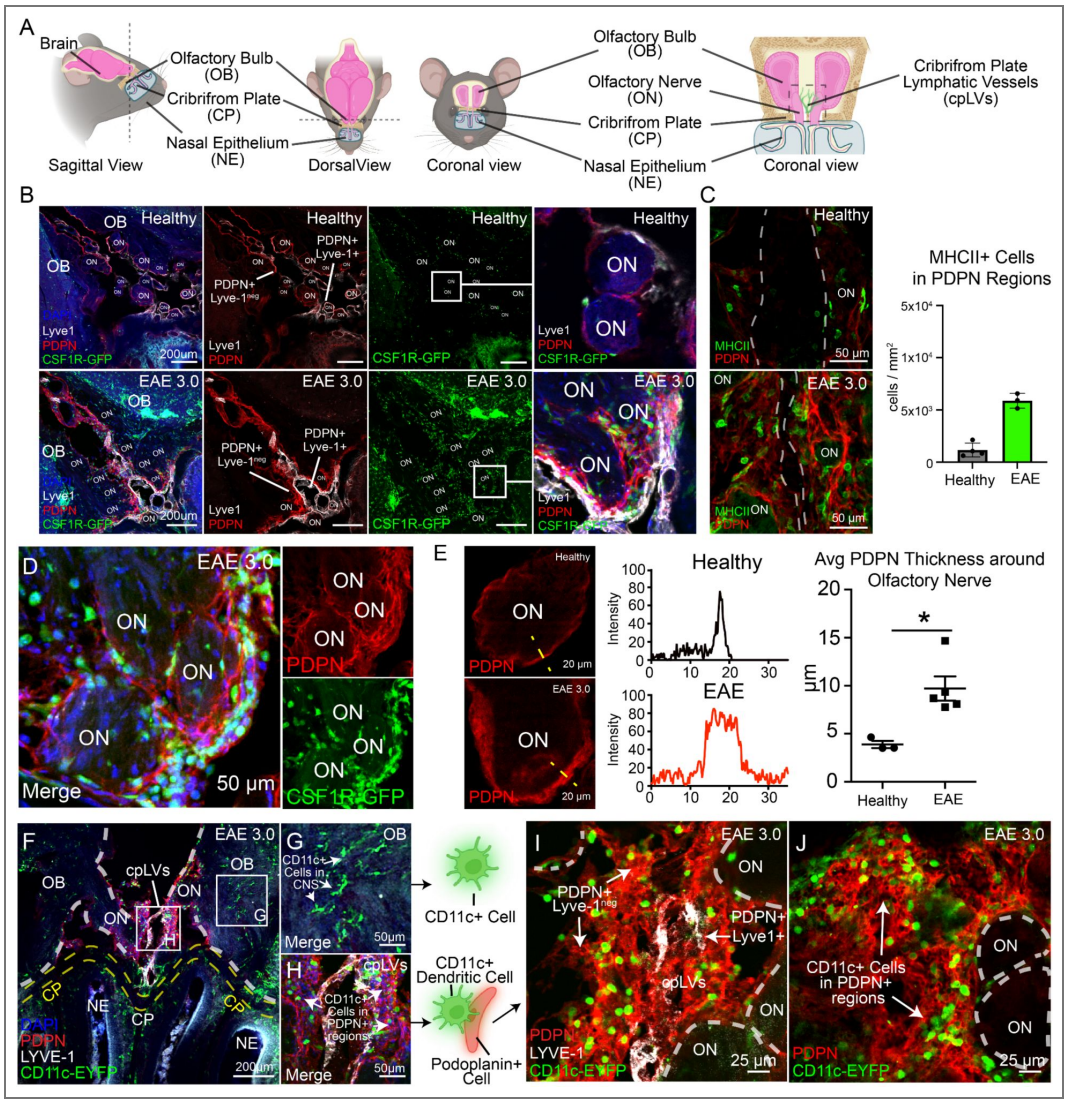

Figure 1. Podoplanin expands and interacts with myeloid cells at the cribriform plate during EAE.

(A): Cartoon schematic of the cribriform plate lymphatic vessels (cpLVs) which associate the perineural environment of olfactory nerves (ON) between the olfactory bulbs (OB) in mice. Lymphatic vessels are directly next to ONs as they project through the cribriform plate (CP) into the nasal epithelium (NE). **(B):** Healthy and EAE 3.0 CSFR1R-GFP mouse CP sections were stained for podoplanin (PDPN) PE and Lyve-1 Alexa 660 to visualize the relationship of myeloid cells (CSF1R-GFP+), lymphatics (Lyve-1+, PDPN+), and meningeal stroma (Lyve-$1_{negative}$, PDPN+). Zoomed panels show the perineural immune-stromal-lymphatic environment around ONs during healthy and EAE. **(C):** Quantification of MHCII MFI at the CP during healthy and EAE 3.0 conditions using identical imaging conditions. MHCII (eFlour 450) increases in PDPN+ regions during EAE. Unpaired student's t-test. **P < 0.01. Data are represented as mean ± SEM. **(D):** Representative image of perineural CSF1R-GFP cells adhered to PDPN+ region of ONs. **(E):** Quantification of average PDPN+ thickness (µm) around ONs during healthy and EAE conditions. Intensity plot profiles (yellow dotted line) were used to estimate PDPN+ regions. n=3-5 mice. *P<0.05. Data are represented as mean ± SEM **(F):** Representative image of immune response at cribriform plate in EAE 3.0 CD11c-eYFP mice stained for Lyve-1 and PDPN. **(G):** Non-Lymphatic ($PDPN_{negative}$, $Lyve1_{negative}$) associated CD11c+ dendritic cells are in the olfactory bulb brain tissue. The cells likely represent infiltrating DCs, macrophages, and activated Microglia. **(H):** Meningeal-Lymphatic ($PDPN^{+}$) associated CD11c+ are at the cribriform plate lymphatics. The cells likely represent infiltrating DCs, macrophages, and monocytes **(I-J):** Representative image of immune response at cribriform plate in EAE 3.0 CD11c-eYFP mice stained for Lyve-1 and PDPN. CD11c-eYFP+ embed into dense PDPN+ ECM) near cribriform lymphatics (Lyve-1).

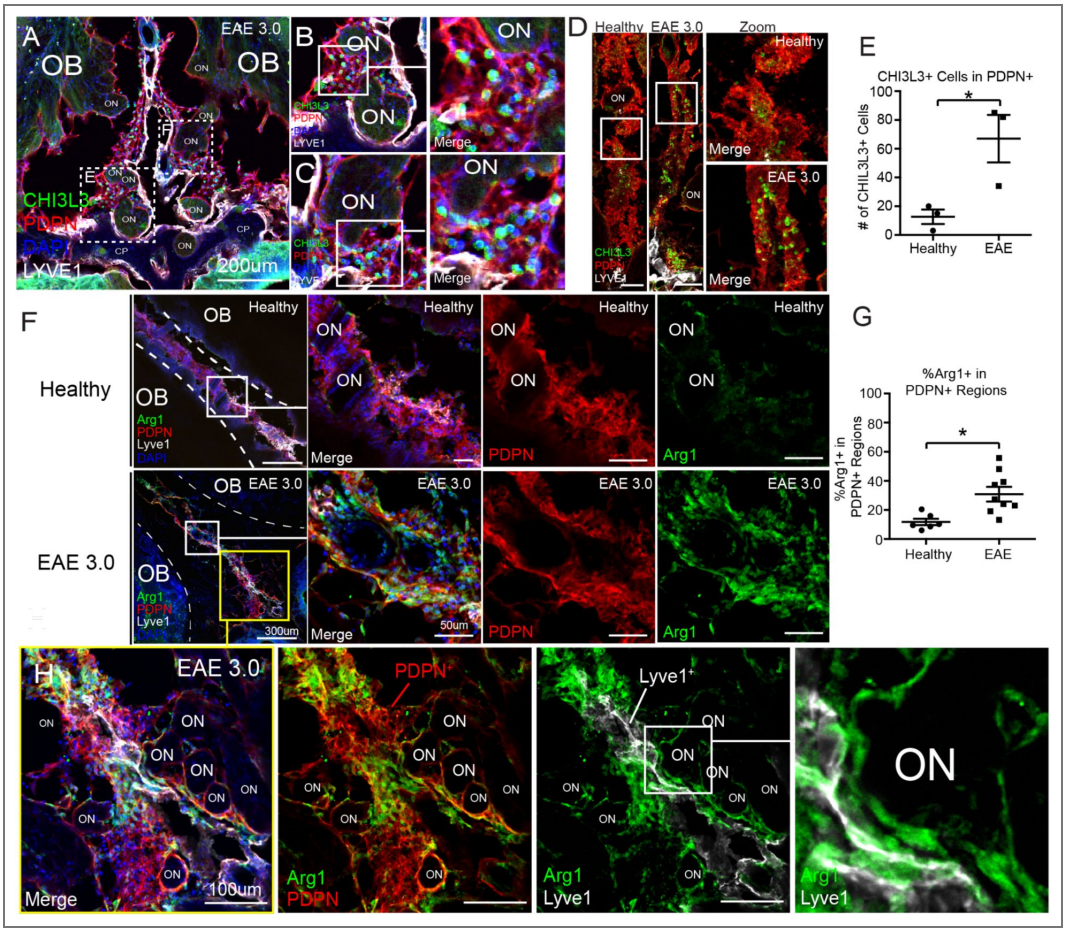

Figure 2. Elevation of CHI3L3 and ARG1 at cribriform lymphatics during EAE

(A-C): Magnification between an EAE 3.0 mouse olfactory bulb (OB) at cribriform plate (CP) showing infiltration of CHI3L3$^+$ cells (green) surrounding olfactory nerves (ON) and localizing within PDPN$^+$ stroma networks (red) and LYVE-1$^+$ lymphatic vessels (white). DAPI marks nuclei (blue). (**B-C**) High-magnification views of boxed regions showing accumulation of CHI3L3$^+$ cells in proximity to ONs and embedded within PDPN$^+$ stromal-lymphatic regions and LYVE-1$^+$ lymphatic zones. **(D-E)**: (**D**) Representative confocal images of healthy and EAE 3.0 tissues showing increase of CHI3L3$^+$ cells (green) in PDPN$^+$ regions during inflammation. **(E)** Quantification of CHI3L3$^+$ cells within PDPN-rich areas, demonstrating significantly elevated numbers in EAE versus healthy controls. Data are represented as mean ± SEM. n = 3 per group **(F-G): (F)** Representative images of ARG1$^+$ (green) immunoregulatory macrophages in healthy and EAE 3.0 mice, showing spatial colocalization with PDPN$^+$ (red) and LYVE-1$^+$ structures (white) near olfactory nerves. Insets highlight increased density and clustering of ARG1$^+$ cells in EAE. **(G)** Quantification of ARG1$^+$ macrophages in PDPN$^+$ regions, showing a significant increase in EAE mice compared to healthy controls ($p = 0.0116$). Data are represented as mean ± SEM. n=6-9 **(H)** High-resolution confocal image of EAE 3.0 olfactory nerve region showing ARG1$^+$ macrophages interacting closely with PDPN$^+$ and LYVE-1$^+$ lymphatics around olfactory nerve bundles (ON). Individual channels shown for ARG1, PDPN, and LYVE-1. Zoomed panel shows perineural ARG1.

Characterization of CD11c$^+$CD11b$^+$ immune cells at the inflamed cribriform plate PME

Leveraging podoplanin as an efficient marker of the non-parenchymal meningeal-lymphatic environment at the cribriform plate (Figure 1), and the established affinity of CD11b$^+$CD11c$^+$ cells to this niche (Hsu et al., 2022), we utilized a doublet sorting approach to enrich cell-cell interactions of interest from inflamed cribriform plate preparations during EAE (Bendall, 2020; Hsu et al., 2022) (Figure 3A). Specifically, we sorted for CD11b$^+$CD11c$^+$ cells, which are bound in PDPN$^+$CD31$^+$ aggregates (Figure 3B; Supplementary Figure 1). We also sorted for singlet CD11c$^+$/CD11b$^+$/CD45$^+$cells and singlet cribriform plate PDPN$^+$/ CD31$^+$/CD45$_{low}$ populations for comparison into a second tube (Figure 3B; Supplementary Figure 1). This procedure yielded a tube of sorted singlet no-contact cells and another tube of aggregating cells in heterotypic interactions. Both tubes were then put through a dissociation procedure using Liberase TL (Roche), which yielded post-contact singlets from the cell aggregates for traditional scRNAseq processing (Figure 3B; Supplementary Figure 1). This method is distinct from physically-interacting cell sequencing (PIC-seq) (Giladi et al., 2020), whereas in PIC-seq, doublet cells are sequenced in active binding events, and then post-sequencing algorithms are used to deconvolute expression data back to single cell resolution. Here, with PostContact-seq the pipeline is more simplified, and in our experiment involves the isolation of newly dissociated myeloid cells which were previously in contact with a PDPN+CD31+ aggregates without the need for deconvolution algorithms. In essence, this process allows us to interrogate the expressional profile of cells with a previously defined affinity for each other.

UMAP analysis revealed 12 distinct clusters (Figure 3C). Overall, no-contact and post-contact clusters had several overlapping cluster classifications (Figure 3C), but had fluctuations in the proportion of immune cells in each cluster (Figure 3D). The heterogeneity of myeloid cells reflects the fact that CD11b and CD11c are present on both resident and infiltrating macrophages in the CNS during neuroinflammation (Jordão et al., 2019; Wlodarczyk et al., 2014; Mrdjen et al., 2018). Notably, the post-contact sample had elevated levels of three macrophage clusters (Mac 1-3), which were characterized by high *Arg1* expression and other commonly reported tissue-repair, remodeling, and debris clearance signatures (*Chil3, Spp1, Mrc1, Apoe, Fn1, Tgfbi)*. Additionally, while the no-contact sample was largely devoid of a T-cell cluster (Cluster 8), the post-contact sample saw a ~13x fold increase in T-cells (Figure 3D). We hypothesize that this could be due to T-cells "hitchhiking" in our sorted aggregates due to their binding affinity to both cell types. While inclusion of post-contact T-cells in the sample preparation was unintended, sequencing revealed aspects of a classical Th1 signature with expression of *Cd3e*, *Cd4*, *Ifng*, *Il2rb*. Of note, one of the most prominent clusters, Cluster 0, expressed CD11c (*Itgax*), but also genes related to CNS resident microglia (*Tmem119*, *P2ry12*, *Siglec-H*) and not the traditional expression signature of dendritic cells (Figure 3E). The presence of microglia in the sorted sample supports the presence of CD11c$^+$ microglia in the CNS during inflammatory disease (Keren-Shaul et al., 2017), which were included in our CD11c$^+$ CD11b$^+$ gating strategy. However, while there was a nearly 50% reduction of this microglia population in the post-contact group (Figure 3D), some of this sorted population could also be derived from nerve bundle resident macrophages, which resemble microglia (Wang et al., 2020).

Additionally, while our results revealed a more heterogeneous CD11b$^+$CD11c$^+$ population than anticipated, our scRNAseq analysis revealed two distinct dendritic cell clusters, which correspond to the traditional expressional signatures of cDCs (Cluster 4: *cD209a*, *Flt3*) and Migratory DCs (Cluster 6: *Ccr7*, *Pdcd1lg2*, *Cd80*, *Cd83*, *Cd200*) (Figure 3E). Migratory DCs expressed several noticeable Th2 response genes, *IL4I1*, *IL4ra*, *Ccl17*, *Ccl22* and *Bcl2l1* (Figure 3E). Broadly, the gene signature of these CCR7$^+$ migratory DCs highly overlapped with published scRNAseq datasets of dendritic cells with a "mregDCs" cell state (or "mature DCs enriched in immunoregulatory molecules") (Maier et al., 2020). This mregDC identity is indicative of a cell state associated with both antigen uptake and maturation but also a restrained stimulatory ability which can be acquired by multiple DC subsets (Maier et al., 2020; Ginhoux et al., 2022).

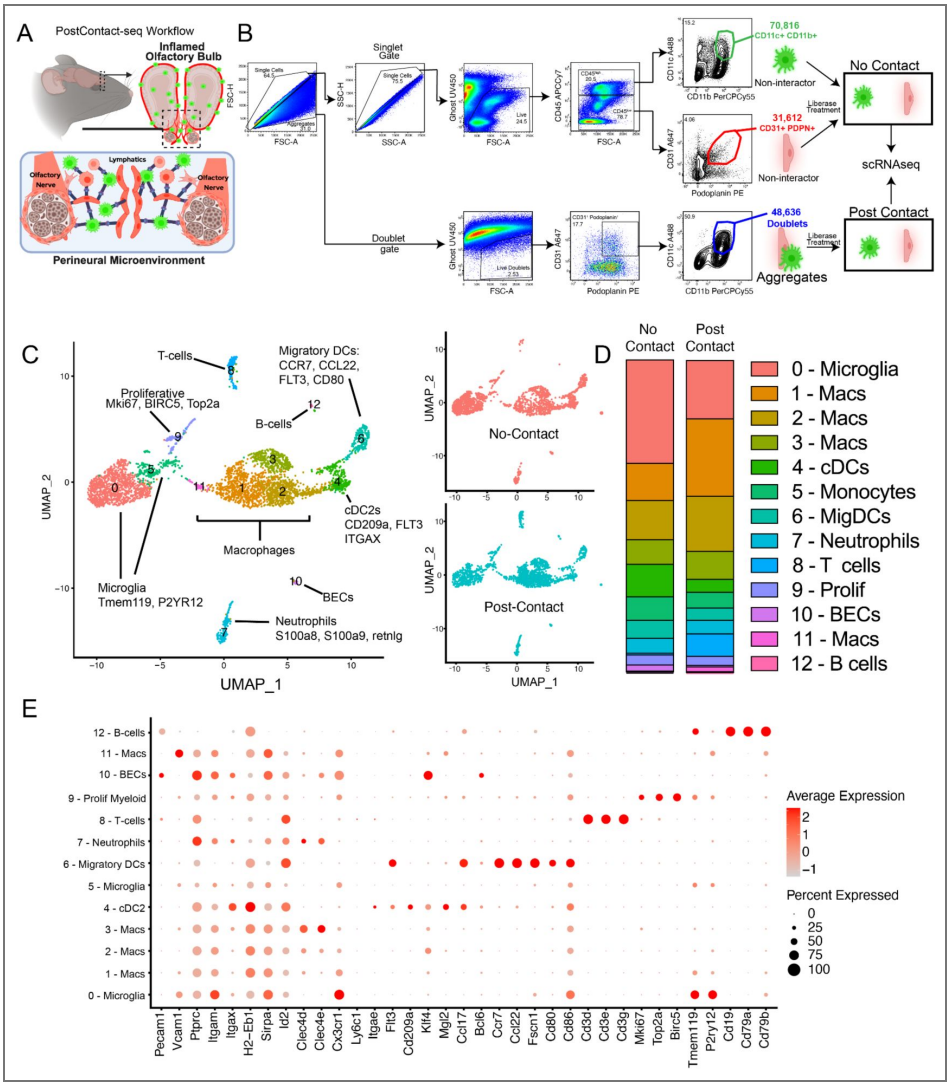

Figure 3. Characterization of post-contact CD11c^{+}CD11b^{+} cells which previously interacted with cribriform plate meningeal-lymphatic niche

(A-B): Cartoon scheme outlining "PostContact-seq" sorting procedure of cribriform plate + Olfactory bulb tissue preparations from EAE 3.0. Sorted singlets from CD11c^{+}CD11b^{+} (Myeloid cells) and CD31^{+}PDPN^{+} (Meningeal-Lymphatic niche) gates were collected into a no-contact tube. Simultaneously, quadruple positive CD11c^{+}CD11b^{+}CD31^{+}PDPN^{+} (Myeloid cell+Meningeal Lymphatic Niche) aggregating cells were sorted into the "interactor" tube. Prior to scRNAseq, both tubes underwent short liberase treatment to dissociate interacting cells and generate single cell suspensions of post-contact, and sequenced. **(C):** Combined UMAP plots show the 12 cluster identities from post-contact and no-contact scRNAseq (Left). Overlaid UMAP plots show the 12 cluster identities from post-contact and non-contact scRNAseq (Right). **(D):** Vertical slice graph shows proportion of each cell cluster between no contact and post-contact tubes. **(E):** Dot plot displays the expression of selected marker genes across cell clusters identified by scRNA sequencing.

Analysis of cribriform myeloid cells supports immunoregulatory retainment at inflamed cribriform plate

To understand the retention of immune cells in the PDPN$^+$ PME, we next investigated specifically the post-contact cells from the scRNAseq dataset for clusters that had measurable expression of *Pdpn*. Again, post-contact which we use here refers to previously PDPN-attached sorted cell aggregates which were dissociated prior for scRNAseq. Interestingly, a subpopulation of fibroblasts that expressed the highest levels of *Ppdn* along with several collagen subunits of the ECM: *Col1a1*, *Col1a2*, *Col6a1*, and *Col6a2* (Figure 4A). To understand what interactions were implicated in our sorted aggregates, we utilized TALKien, a cell interaction analysis to understand the broad profile of cell-cell crosstalk among cells in the post-contact clusters (Figure 4B) (Moratalla-Navarro et al., 2023). Importantly, this integrated analysis utilizes Ligand-Receptor databases from CellChat, CellPhoneDB, iCellNet, and Ramilowsky datasets (Moratalla-Navarro et al., 2023). Cell interaction analysis predicted high levels of crosstalk between macrophages-fibroblasts and macrophages-migratory DC subsets (Figure 4B-C). Importantly, this analysis agrees with our immunohistochemistry analysis of the inflamed cribriform plate environment that displays a dense PDPN$^+$ meningeal lymphatic environment with interacting myeloid cells (Figure 4D, Figure 1B-J). Gene ontology analysis of potential interactions pointed to several ECM pathways, but also IL-10 signaling pathways (Figure 4E).

Additionally, Th2-skewed macrophages are characterized by high expression *Arg1*$^+$/*Chil3*$^+$ and are the dominant post-contact cluster in our dataset (Figure 4F, Supplemental Figure 3) and previously found to increase at cribriform plate (Figure 2). Interestingly, post-contact macrophages (Cluster 2) have lower expression of MHC-II antigen processing and presentation genes (*H2-DMa*, *H2-Aa*, *H2-Ab1*, *H2-DMb1*, *H2-Eb1*, *Cd74*, *Ciita*) and elevated expression of *Chil3*, *Sdc4*, and *Spp1* key ECM related binding proteins (Figure 4G). This population also expressed *Ccr2* and *Cxcr4* (Figure 4F), implicating monocyte recruitment to cribriform plate may occur via classical CCL2-CCR2 and CXCR4-CXCL12 axis to the ECM meningeal regions. In agreement with this CCR2$^+$ cells increased significantly in PDPN$^+$ regions between olfactory bulbs during EAE, even appearing to embed into a PDPN$^+$ ECM (Supplemental Figure 4A-C). In agreement with an alternatively activated phenotype, enriched gene ontology pathways for post-contact macrophages included homotypic cell adhesion (*Pdpn*, *Emilin2*, *Lgals1*, *Plaur*), ECM-formation (*Ecm1*, *Tgfbi*, *Emilin2*, *Fn1),* negative regulation of IL-12 production, and negative regulation of cytokines in immune response (Figure 4H).

Cribriform DCs have enrichment pathways related to reduced pro-inflammatory signature and *Pdcd1* (PD-1) expression

CCR7$^+$ migratory DCs (cluster 6) were a key post-contact subset in our data set, and MHCII$^+$ cells were heavily implicated in our IHC analysis (Figure 5A). Enriched pathways in cluster 6 DC included positive regulation of cell adhesion, negative regulation of immune system processes, and positive regulation of programmed cell death (Figure 5B). Overall, post-contact and no-contact DCs shared a highly overlapping signature, but further comparison of enrichment pathways from the top 300 gene list of no-contact and post-contact DCs revealed several unique pathways within the post-contact DCs including, programmed cell death, caspase activation, tolerance induction, and response to L-arginine (Figure 5C). Inversely, we saw several unique pro-inflammatory gene enrichment pathways in the no-contact DCs, including positive regulation of IL12 and IL17 signaling (Figure 5C).

Focusing on programmed cell death pathways, we next sought to identify all the immune cells within our scRNAseq dataset that express *Pdcd1*, the gene which encodes programmed cell death receptor 1 (PD-1), a well-characterized checkpoint inhibitor receptor expressed in activated infiltrating CD4 T-cells during EAE (Schreiner et al., 2008). While *Pdcd1* was expressed in the post-contact T-cell cluster (Cluster 8), it was also detectable in the CCR7+ migratory DCs (Cluster 6) (Figure 5D). Furthermore, when we further divided the data into “post-contact” vs “no-contact” clusters, we noticed that *Pdcd1* was primarily expressed by the post-contact migratory DCs (Figure

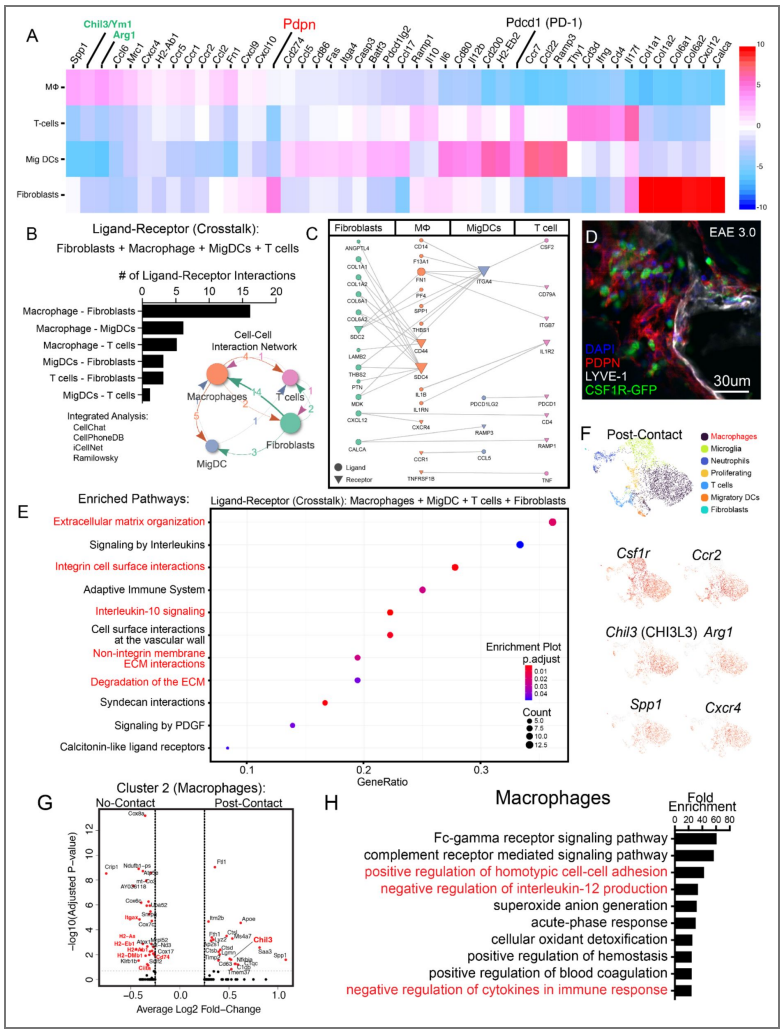

Figure 4. Analysis of post-contact cells reveals immune cell and extracellular matrix crosstalk

(A) Heatmap displaying scaled expression (z-score) of highly expressed representative genes involved in immune regulation, immune activation (e.g., *Pdcd1*) across four cell types: macrophages (MΦ), T cells, migratory dendritic cells (Mig DCs), and fibroblasts (e.g., *Pdpn*). Color scale indicates expression levels. **(B)** Quantification and network map of predicted ligand-receptor interactions between fibroblasts and immune populations (macrophages, Mig DCs, and T cells) using integrated analysis from CellChat, CellPhoneDB, iCellNet, and the Ramilowsky dataset. The bar graph shows the number of unique ligand-receptor interactions per pairwise combination, with the most extensive communication observed between macrophages and fibroblasts. Analyzed with crossTALK IntEraction Network (TALKIEN) (Moratalla-Navarro et al., 2023) with microglia, neutrophils, and proliferating gene sets excluded. **(C)** Network plot illustrating specific ligand-receptor pairs involved in fibroblast-immune cell communication. Arrows point from ligand-expressing to receptor-expressing cell types. Notable interactions include *Spp1-CD44*, *Pdpn-Clec2d*, and *Thbs1-CD47*. **(D)** Immunofluorescence imaging of the cribriform plate region in EAE day 3.0 mice showing spatial organization of LYVE-1$^+$ lymphatics (white), PDPN$^+$ lymphatics and ECM (red), and CSF1R-GFP$^+$ myeloid cells (green). DAPI (blue) marks nuclei. Scale bars: 30 µm. **(E)** Pathway enrichment analysis of ligand-receptor pairs among macrophages, Mig DCs, T cells, and fibroblasts. Enriched pathways include extracellular matrix organization, integrin-mediated interactions, interleukin 10 signaling. Gene ratio represents the proportion of identified genes contributing to each pathway; dot size reflects the number of genes, and color indicates adjusted p-value. **(F) :** UMAP projection shows major post contact cell types, including macrophages (purple), microglia (green), neutrophils (blue), T cells (orange), proliferating cells (light blue), migratory dendritic cells (yellow-orange), and fibroblasts (aqua). Feature plots highlight expression of *Chil3* (CHI3L3), *Arg1*, *Spp1*, *Ccr2*, *Cxcr4*, *Csf1r* **(G) :** Volcano plot comparing post-contact vs no-contact cluster 2 macrophages (Highest *Arg1* expressing cluster). Analysis reveals post contact macrophage have downregulated MHC-II processing and presentation genes (*H2-DMa*, *H2-Aa*, *H2-Ab1*, *H2-DMb1*, *H2-Eb1*, *Cd74*, *Ciita*) and elevated expression of *Chil3* (CHI3L3), another alternatively activated macrophage marker and ECM binding protein. **(H) :** Gene ontology enrichment analysis (bottom) demonstrates post contact Macrophages are enriched for pathways in Fcγ receptor and complement receptor signaling, negative regulation of IL-12 production, homotypic cell-cell adhesion, and hemostasis.

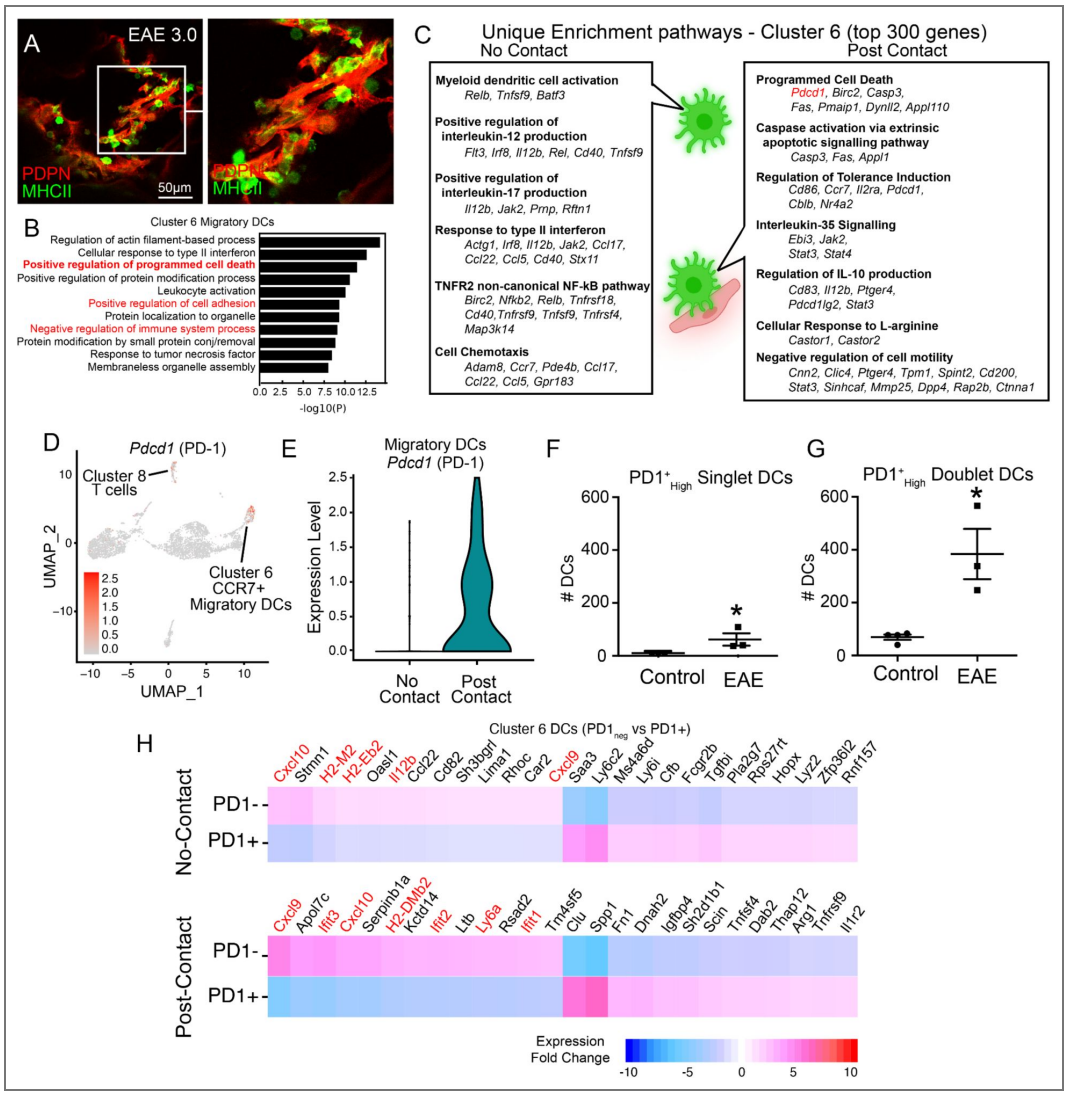

Figure 5. Post-Contact DCs have pathways related to reduced pro-inflammatory signature and *Pdcd1* (PD-1) expression

(A) High-resolution confocal image from EAE 3.0 CP showing MHCII⁺ (green) cells in close proximity to PDPN+ stroma (red). **(B)** Gene ontology enrichment analysis of cluster 6 migratory DCs reveals pathways related to actin dynamics, interferon signaling, leukocyte activation, and programmed cell death. Red text indicates immune pathways of interest. **(C)** Comparison of unique enrichment pathways from top 300 genes compared between no-contact and post-contact DCs. **(D)** UMAP visualization of scRNA-seq data highlighting *Pdcd1* (PD-1) expression in cluster 6 CCR7⁺ migratory DCs and cluster 8 T cells **(E)** Violin plot showing *Pdcd1* expression in post contact DCs versus no-contact, suggesting PME influence on DC checkpoint expression. **(F-G)** Quantification of PD-1^{High} single and doublet DCs at the olfactory-cribriform junction, showing significant increase in EAE mice compared to controls. n = 3, unpaired Student's t-test. Data are represented as mean ± SEM. Singlet DCs (p=0.0322), Doublet DCs (p=0.0084). **(H)** Heatmaps of highest genes expressed genes in PD-1⁺ vs PD-1⁻ DCs within CD31+PDPN+ post-contact and no-contact subsets. Pro-inflammatory genes (*Cxcl10*, *Il1b*, *Ifit1, Ifit2, Ifit3*.) are high in PD-1 negative DCs.

5E). Using a minimum threshold of 0.5 *Pdcd1* expression level, we estimated that around 45.8% of the post-contact migratory DCs were positive for *Pdcd1* expression, whereas <15% of no-contact migratory DCs were PD-1^{+}. To verify surface level expression of PD-1 on cribriform migratory DCs during neuroinflammation, we next performed flow cytometry analysis on leukocytes in cribriform plate cell suspensions during EAE and steady state. Here, similar to the scRNAseq experiment, we gated for singlet and doublet CD11c^{+} CD11b^{+} CD45^{+} DCs and identified that singlet DCs in our cribriform plate preparation contain PD-1 at detectable levels during EAE, and that doublet DC aggregates expressed PD-1 (Figure 5F-G, Supplemental Figure 2).

Engagement of PD-1 on myeloid cells, including DCs, has been shown to inhibit interferon (IFN) signaling pathways through the activation of SHP-2 (Knutson, 2024; Klement et al., 2023). This inhibition in DCs has been shown to lead to reduced production of pro-inflammatory chemokines and cytokines mainly: CXCL9, CXCL10, and IL12B, which are crucial for pro-inflammatory T cell recruitment and initiating Th1 immunity by DCs (Knutson, 2024; Klement et al., 2023). To better understand the inflammatory profile of PD-1^{+} DCs at the cribriform plate, we compared the expression signature of PD-1 expressing and non-expressing CCR7^{+} DCs from cluster 6 of our datasets (Figure 5H). Highest genes in PD1^{negative} DCs included chemokines *Cxcl9*, *Cxcl10*, *Il12b*, interferon-Stimulated Genes (*Ifit1*, *Ifit2*, *Ifit3*), and several MHC-related genes (*H2-M2*, *H2-Eb2*, *H2-DMb2)* (Figure 5H). Together, these data support that migratory DCs expressing *Pdcd1* exhibit an immunosuppressive gene signature which has been recently described in myeloid cells, including DCs, in tumor microenvironments (Knutson, 2024; Klement et al., 2023). Our data extends these described characteristics of PD-1+ DCs to the cribriform plate drainage environment during EAE-induced autoimmunity.

Peripheral blood derived DCs undergo cell death at cribriform plate-lymphatic niche during neuroinflammation

Since some DCs displayed some unique pathways related to programmed cell death and apoptosis, we next sought to better understand the kinetics of recruitment and death of CD11c^{+}CD11b^{+} cells at the cribriform plate lymphatic niche during EAE. To do this, we utilized a method of CD45 intravascular staining (CD45-IV) to tag blood-originating leukocytes and track their migration into the olfactory-cribriform plate axis. This IV-staining method originally, established by *Anderson et al.*, can label ~99% of leukocytes in the blood within 3 minutes of injection; these labeled leukocytes can then be tracked out of the blood and quantified in tissues across time (Anderson et al., 2014). Using a retro-orbital injection, we IV-stained peripheral blood CD45^{+} immune cells at several time points prior to tissue collection (3 minute, 6, 9,12, 18, 24, 48 hrs). Then we investigated the presence of CD45 IV^{+} DCs bound to CD31^{+}PDPN^{+} aggregates at the cribriform plate (Figure 6A; Supplementary Figure 5). Here, we found that at the 3-minute time point, very few of the doublets (<1%) originated directly from the blood in our sample preparation (Figure 6A), indicating that there is minimal contamination from blood. Interestingly, between 24-48 hours after IV-injection, the total percentage of CD45IV^{+} stained DCs increases steadily (Figure 6B), highlighting a time-dependent relationship to CD11c^{+}CD11b^{+}PDPN^{+}CD31^{+} binding events. We also determined that doublets had increasing Ghost^{+} cells across time, which suggests cells are dying in a time-dependent relationship (Figure 6C). To validate the apoptotic potential of DCs at the cribriform plate, we stained EAE sections from CD11c-eYFP mice with Cleaved Caspase-3 and Lyve-1 (Figure 6D), where we confirmed Cleaved-Caspase-3^{+} DCs in an active binding interaction with Lyve-1 (Figure 6D).

Finally, we analyzed the viability of PD-1^{+} DC doublet aggregates using flow. We determined that PD-1^{+} aggregates had a higher percentage of Ghost^{+} cells when compared PD1^{neg} DC doublet aggregates, suggesting PD-1^{+} DCs undergo cell death in engagement with this niche (Figure 6E). Together, these data support that blood-derived CD11c+ DCs can migrate to the cribriform plate PME regions in a time-dependent manner, with subpopulations dying as they interface with the meningeal-lymphatic environment.

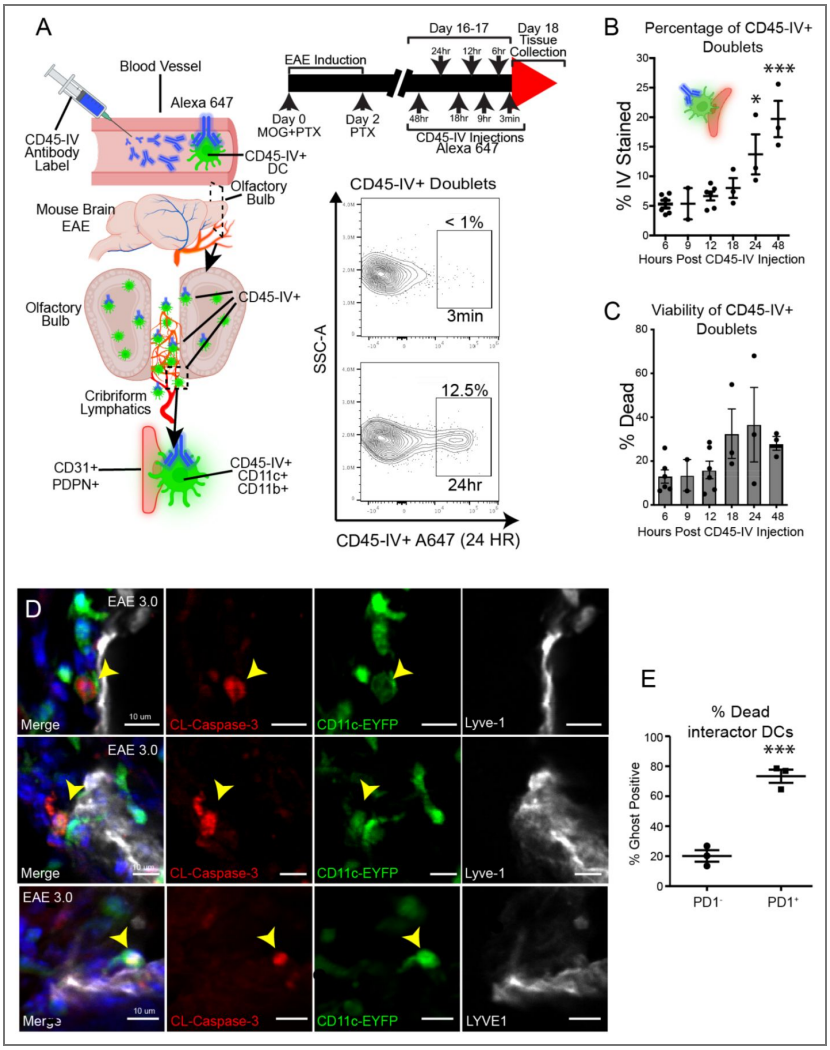

Figure 6. Blood-derived CD11c+CD11b+ cells migrate to cribriform plate lymphatics in a time dependent manner and undergo cell death

(A) Schematic overview of experimental design. Mice were intravenously injected with Alexa Fluor 647-labeled CD45 antibody (CD45-IV) at multiple timepoints following EAE induction to label blood-accessible leukocytes. Diagram (left) shows DC trafficking to the cribriform plate niche. Representative flow plots (right) show the lack of CD45-IV$^+$ doublets at 3 minutes and emergence of IV+ cells at 24 hours post-injection. **(B)** Quantification of the percentage of CD45-IV$^+$ CD11c+CD11b+CD31+PDPN+ doublets over time, showing progressive accumulation of stained doublets, peaking at 48 hours post-injection. 24 hr (p=0.0227) and 48 hr (p=0.0001) time points are significantly elevated when compared 6 hr. One way anova with Tukey's multiple comparison. Data combined from 3 independent experiments. Data are represented as mean ± SEM n=2-6 per group **(C)** Viability of CD45-IV$^+$ doublets assessed by live/dead staining at different timepoints, showing trend of cell death (Ghost+) over time. One-way anova (P = ns). data are represented as mean ± SEM n=2-6 per group **(D)** Representative confocal images from EAE 3.0 mice showing cleaved caspase-3$^+$ (red) CD11c-EYFP$^+$ DCs (green) interacting with LYVE-1$^+$ lymphatics (white). Yellow arrowheads highlight apoptotic DCs. **(E)** Quantification of Ghost+ cells among PD-1$^-$ and PD-1$^+$ DCs identified as interactors, showing significantly higher cell death among PD-1$^+$ interactor doublets. n = 3, P = 0.0008, unpaired Student's t-test. Data are represented as mean ± SEM.

Discussion

Drainage of cerebrospinal fluid (CSF) and its associated inflammatory cues are essential for maintaining CNS fluid homeostasis, clearing waste, and coordinating neuroimmune responses with the periphery (Kipnis, 2024). Recent work by our lab and others has demonstrated that lymphatic vessels associate with CSF-interfacing olfactory nerve bundles at the cribriform plate and undergo dynamic remodeling during neuroinflammation, where they undergo lymphangiogenesis, facilitate antigen drainage, and upregulate transcriptional programs linked to leukocyte cross-talk (Hsu et al., 2022, 2019; Spera et al., 2023; Decker et al., 2022; Xin et al., 2024). Previously, we determined that the cribriform plate niche is dominated by interacting $CD11c^{+}CD11b^{+}$ myeloid cells (Hsu et al., 2022) with access to nearby skull bone marrow via perineural bone channels (Laaker et al., 2025). Together, these findings support the concept that the perineural microenvironment (or PME) at the cribriform plate functions as a specialized immunoregulatory interface, linking the previously described CSF-to-lymphatic drainage with the recruitment, retention, and programming of PME myeloid cells.

In this study, we isolated $CD11c^{+}CD11b^{+}$ cells in contact with $PDPN^{+}CD31^{+}$ aggregates from inflamed cribriform plate preparations, dissociated cells from their ongoing cell-cell interactions, and then analyzed their residual post-contact gene expression profile compared to non-interacting controls. Our analysis revealed several immune cell interactions but suggested a high number of macrophage, migratory DC, and fibroblast (ECM) interactions. Additionally, no-contact DCs had unique pathways more characteristic of activated DCs, including IL-12, IL-17 production, and levels of chemokine receptors. In contrast the post-contact migratory DCs were enriched with pathways related to immune tolerance, reduced cell motility, and programmed cell death including the expression of the inhibitory receptor *Pdcd1* (PD-1). In summary, retained DCs had more regulatory and sessile characteristics from our analysis.

While many potential interaction pathways emerged, we decided to interrogate programmed cell death and Th2-skewed immune responses at the cribriform plate. Interestingly, in EAE, $PD\text{-}1^{+}$ DCs accumulated at higher levels at the cribriform plate region, and PD-1 expression had a signature associated with inhibited interferon signaling. Immunosuppressive signatures extended to macrophage subsets too, with elevated $ARG1^{+}/CHI3L3^{+}$ alternatively activated macrophages accumulating in these $PDPN^{+}$ regions during EAE. Together, our findings support the establishment of an immunosuppressive myeloid network in the $PDPN^{+}$ ECM surrounding CSF-effluxing and lymphatic interfacing olfactory nerve bundles (Supplemental Figure 6).

Previously, our lab showed that *Cd274* (PD-L1), the ligand for PD-1, increases in the cribriform plate lymphatic niche during EAE, suggesting neuroinflammation promotes suppressive PD-L1/PD-1 crosstalk at this site (Hsu et al., 2022). Additionally, Pdcd1lg2 (PD-L2), Cd80, and Cd83 by migratory DCs likely reflects a tolerogenic activation state rather than a conventional immunostimulatory. While PD-1's inhibitory role on effector responses in T-cell subsets has been extensively studied, its role in DCs is considerably less understood, though documented in several disease contexts. For example, $PD\text{-}1^{+}$ DCs have been identified in the tumor microenvironment (TME) in both human and animal studies (Karyampudi et al., 2016; Strauss et al., 2020; Kwiecień et al., 2022; Lim et al., 2016; Krempski et al., 2011; Wang et al., 2022b; Gordon et al., 2017). Similar to its function in T-cells, PD-1 on DCs has been implicated as highly inhibitory, reducing DC stimulatory ability and survival, and negatively influencing tumor response (Karyampudi et al., 2016). Inversely, eliminating PD-1 in *Pdcd1* KO, APCs exhibit an increased ability to activate T-cells in a tumor model, resulting in better tumor control (Strauss et al., 2020). Interestingly, Park and colleagues showed that *Pdcd1*-KO DCs were less likely to be apoptotic and were able to evoke higher antigen-specific T cell responses (Park et al., 2014). Thus PD-1 appears to be a useful receptor to identify subsets of inhibited DCs. In agreement with this, our data support that *Pdcd1*-expressing DCs also have low levels of *Cxcl9*, *Cxcl10*, *Il12b,* and several antigen presentation and processing genes. PD-1 engagement by PD-L1 has been proposed

to suppress IFN-signaling pathways in DCs through the SHP-2 pathway (Knutson, 2024; Lamichhane et al., 2017). In line with this, several Interferon-Stimulated Genes (*Ifit1*, *Ifit2*, *Ifit3*) were lower in PD-1$^+$ DCs in the cribriform plate dataset.

While the induction pathways of *Pdcd1* in DCs is not fully elucidated, evidence suggests that sustained IL-10 secretion from nearby myeloid cells (Macrophages and/or MDSCs) is a key pathway that upregulates the PD-1 receptor on DCs (Knutson, 2024; Lamichhane et al., 2017). Notably, IL-10 secretion is commonly associated with ARG1+ / CHI3L3+ producing macrophage subsets, which we identified both in our scRNAseq dataset and in IHC analysis of PME-interacting cells. Additionally, our data supports that Arg1$^+$ macrophages express PDPN as well (Zhang et al., 2025a; Wu et al., 2024), contributing to niche complexity. Analysis suggests that IL-10 and ECM remodeling pathways are enriched in the immune-stromal environment surrounding olfactory nerves. In models of sciatic nerve injury, infiltrating monocyte-derived macrophages are recruited and retained perineurally, adopting an *Arg1*$^+$ / *Chil3*$^+$tissue repair-associated program, which is distinct from resident macrophage subsets (Ydens et al., 2020). Thus, our observation of a similar type 2 skewed immunoregulatory niche around olfactory nerve bundles may also promote local tissue remodeling and immunosuppression at the cribriform plate PME, a known site of CSF and antigen drainage(Hsu et al., 2022; Laaker et al., 2025).

In a previous study, we identified in mice that CSF-interacting olfactory nerve bundles have connections to a nearby pool of ethmoid bone marrow (Laaker et al., 2025). During EAE, CSF1R-GFP$^+$ immune cells could be observed traversing these skull channels, providing a potential pathway for local recruitment and coordination of myeloid immune responses to the PME (Laaker et al., 2025). As a result, CCR2+ monocytes and CCR7+ DCs may migrate or mature at the cribriform plate lymphatic region and adopt these tolerogenic characteristics.

Similar immunosuppressive stromal-lymphatic environments are also commonly reported in tumor microenvironment (TME), and are known to promote suppressive macrophages and tolerogenic DCs (Swartz and Lund, 2012; Bieniasz-Krzywiec et al., 2019; Xiao et al., 2023). Additionally, local metabolic shifts in the TME have been implicated as a driver of tolerogenic DC cell states (Snyder and Amiel, 2018). Direct depletion of nutrients such as arginine by M2 macrophages and MDSCs can lead to mTOR inactivation in DCs, which directly reduces DC stimulatory ability (Turnquist et al., 2007; Sukhbaatar et al., 2016; Reichardt et al., 2008; Mondanelli et al., 2017). Future studies will investigate which factors can most reliably influence a broad immunosuppressive environment surrounding CSF-nerve drainage sites. These factors include TGF-β, which is also secreted by alternatively activated macrophages and has been shown to highly induce meningeal stroma thickening and suppress antigen outflow from meningeal lymphatics (Hitpass Romero et al., 2025).

There are several limitations to our investigation. For one, our sequencing approach prioritized myeloid cell-cell interactions, and reduced the acquisition of important stromal and endothelial cell populations in downstream sequencing. Additionally, due to anatomical constraints of the region, we did not perform any selective targeting or depletion of these myeloid cell populations. Future investigations will attempt to selectively inhibit the cribriform myeloid populations to alter disease pathogenesis and utilize complementary approaches like PIC-seq to compare methodology. In addition, we opted to look at a single timepoint of neuroinflammation at peak EAE.

In summary, our findings support that the cribriform plate lymphatic region is a dynamic site of myeloid cell regulation, which is enriched for Th2-skewed macrophages and a subpopulation of migratory DCs with a tolerogenic signature during EAE. Given cribriform lymphatic vasculature facilitates DC drainage to cervical lymph nodes (Hsu et al., 2019, 2022; Jin et al., 2025; Yoon et al., 2024), these findings could be important for altering DC phenotypes and coordinating peripheral immune responses. Our data also highlights the complexity of the cribriform plate region, with the integration of anti-inflammatory macrophages, which likely play a role in protecting local nerve health, promoting tolerance and modulating lymphatic outflow of region (Hsu et al., 2022; Choi et al., 2025; Hsu et al., 2019). These results raise the question of if targeted delivery of immunotherapies at DC efflux sites and immune hub regions could promote more efficent CNS immune response during diseases like brain cancer, Alzheimer's, or CNS

infection (Li et al., 2023). Inversely, enhancing the immunosuppressive capabilities at skull foramina sites may be a new aspect of treating CNS autoimmunity. However, comparable anatomical and immunoregulatory relationships need to be fully investigated in humans. Future studies will attempt to test this framework to understand how drainage sites can tune APCs for downstream impacts on peripheral immunity and further elucidate the unique features of these environments (Hsu et al., 2022; Laaker et al., 2025).

Materials and Methods

Animals

Female C57BL/6J wild-type (stock #: 000664) and CSF1R-GFP MacGreen mice (stock #: 018549), were purchased from Jackson Laboratories. CD11c-eYFP transgenic reporter mice were a generous gift from Dr. Michel C. Nussenzweig at Rockefeller University. Eight to twelve-week old female mice were used for all EAE experiments. All experiments were conducted in accordance with guidelines from the National Institutes of Health and the University of Wisconsin, Madison Institutional Animal Care and Use Committee.

EAE Induction

EAE was induced in 8 to 12-week-old female mice by subcutaneous immunization with 100 μg of MOG_{35-55} emulsified in Complete Freund's Adjuvant (CFA) between the shoulder blades. 200 ng of Pertussis Toxin (PTX) was injected intraperitoneally at 0 days post immunization (d.p.i.) and 2 d.p.i. The onset of clinical scores were observed between day 8 and 12 post-immunization, and were assessed daily as follows: 0, no clinical symptoms; 1, limp/flaccid tail; 2, partial hind limb paralysis; 3, complete hind limb paralysis; 4, quadriplegia; 5, moribund. Intermediate scores were also given for the appropriate symptoms. An EAE clinical score between 2.5-3.5 at day 15 to 18 post-immunization was used for all experiments.

Histology

Mice were terminally anesthetized with isoflurane and transcardially perfused with 0.1M PBS followed by perfusion with 4% paraformaldehyde (PFA) in 0.1M PBS. Mice were then decapitated and the skin surrounding the head was removed using forceps and scissors to separate the skin from the muscle and ear canal. The whole heads were fixed in 4% PFA in 0.1M PBS overnight. The whole heads were then decalcified in 14% ethylenediaminetetraacetic acid (EDTA) in 0.1M PBS for 7 days followed by cryoprotection in 30% sucrose in 0.1M PBS for 3 days. The EDTA was replaced with fresh 14% EDTA each day. The decalcified mouse heads were then embedded in Tissue-Tek OCT Compound, frozen on dry ice, then stored at -80°C. 60 μm thick frozen sections were obtained on a Leica CM1800 cryostat, mounted on Superfrost Plus microscope slides and stored at -80°C. For dural tissues, the skullcap was isolated and collected after decalcification and stored at 4°C in a 48-well non-tissue culture treated plate containing PBS.

Immunohistochemistry

Sections were thawed at room temperature for 10 minutes, washed with 0.1M PBS for 10 minutes, then unspecific binding blocked with 10% bovine serum albumin (BSA) with 0.1% Triton-X for permeabilization in 0.1M PBS for 60 minutes. Sections were then incubated with the appropriate primary antibodies in 1% BSA and 0.1% Triton-X in 0.1M PBS at 4°C overnight in a humidified chamber. The following antibodies were used for immunohistochemistry: Podoplanin PE (eBioscience, Catalog #: 12-5381-80), CD31 Alexa647 (BD Biosciences, Catalog #: 563608), Lyve-1 eFluor660 (Thermo Fisher Scientific, Catalog #: 50-0443-80), MHC II eFluor450 (eBioscience, Catalog #: 48-5321-80), CD11c Alexa488 (Thermo Fisher Scientific, Catalog #: 53-0114-80), YM1 / CHI3L3 (R&D Systems Catalog #: AF2446), Arginase-1 (Invitrogen, Catalog #: PA5-29645), Cleaved Caspase-3 (Abcam, Catalog #: E83-77). Sections were then washed three times with 0.1M PBS for 10 minutes each, then incubated with the appropriate secondary antibodies in 1% BSA and 0.1% Triton-X in 0.1M PBS at room temperature for 120 minutes. The following secondary antibodies were used:

Donkey anti-Chicken Alexa488 (Invitrogen, Catalog #: A11039), Donkey anti-Chicken Alexa647 (Invitrogen, Catalog #: A21449), Donkey anti-Goat Alexa568 (Invitrogen, Catalog #: A11057), and/or Donkey anti-rabbit Alexa568 (Invitrogen, Catalog #: A10042). Sections were then washed three times with 0.1M PBS for 10 minutes each, mounted with Prolong Gold mounting medium with DAPI, and images acquired using an inverted Olympus Fluoview FV1200 confocal microscope.

Single Cell Suspension Preparation

Mice were terminally anesthetized with isoflurane and transcardially perfused with PBS. Mice were then decapitated, and the skin was cut dorsal to the midline of the skullcap rostrally to expose the brain. The skullcap was then removed along with the brain and dura after separation from the olfactory bulbs. The cribriform plate and its associated tissues, which included portions of the olfactory bulbs and the cribriform plate, were dissected out and placed in a 70-micron strainer submerged in RPMI-1640 in a non-tissue culture treated dish. The tissues were then mechanically dissociated by pushing the tissue through the strainer using a syringe plunger. The mechanically dissociated cells were then spun down, washed, and resuspended in FACS buffer (1% Bovine Serum Albumin in 0.1M PBS) for FACS staining.

Flow Cytometry

After resuspension of mechanically dissociated cells in fluorescence-activated cell sorting (FACS) buffer (pH = 7.4, 0.1M PBS, 1 mM EDTA, 1% BSA), the cells underwent staining with conjugated antibodies/dyes. Conjugated antibodies were diluted 1:200 in FACS buffer, and the following antibodies and dyes were used: Ghost UV450 (Tonbo Biosciences, Catalog #: 13-0868-T500) or Ghost Violet540 (Tonbo Biosciences, Catalog #: 13-0879-T100) to visualize live/dead cells; CD31 Alexa647 (BD Biosciences, Catalog #: 563608), Podoplanin PE (eBioscience, Catalog #: 12-5381-82), CD45 APC-Cy7 (Biolegend, Catalog #: 103116) or CD45 APC eFluor780 (eBioscience, Catalog #: 47-0451-80) to visualize leukocytes; CD11b PerCP-Cy5.5 (Biolegend, Catalog #: 101227) or PE (Invitrogen, Catalog #:12-0112-82), CD11c Alexa488 (Invitrogen, Catalog #: 2284135), or CD11c FITC (Biolegend, Catalog #: 117305) to visualize dendritic cells; PD-1 BV421 (Biolegend, Catalog #: 109121), CD4 A647 (BD Biosciences, Catalog #: 557681). After staining for 30 minutes at 4°C, cells were washed 3 times with FACS buffer and run using Cytek's 3-laser Northern Lights.

FACS Sorting

After generating a single cell suspension and staining for cribriform plate with Ghost UV450 (Tonbo Biosciences, Catalog #: 13-0868-T500), CD31 Alexa 647 (BD Biosciences, Catalog #: 565608), Podoplanin PE (eBioscience, Catalog #: 12-5381-82), and CD45 APC-Cy7 (Biolegend, Catalog #: 103116), the cells were sorted with a FACS Aria III with a nozzle size of 130 um at the UW Flow Core satellite facility in the UW Biotechnology Center. Cells were gated for singlets using both FSC and SSC, dead cells excluded by gating for Ghost^{negative} live cells, and were identified using both CD31^{+} Podoplanin^{+} after excluding both CD45^{intermediate} microglia and CD45^{+} leukocytes as previously described(Hu et al., 2020; Herz et al., 2018; Louveau et al., 2015; Da Mesquita et al., 2018). Cells were sorted into either FACS buffer (1% BSA in PBS) for scRNA-seq, or RPMI containing 10% FBS, 2-mercaptoethanol, and penicillin/streptomycin for *in vitro* co-culture experiments.

scRNA Sequencing

A single cell suspension of the cribriform plate was generated from 8 pooled EAE mice and FACS sorted for singlets, Ghost^{-} live cells, CD45$_{low}$, Podoplanin^{+}, and CD31^{+}. Sorted cell suspensions were then provided to the Biotechnology Core facility at the University of Wisconsin Madison for single cell sequencing using the 10x Genomics Chromium Single Cell Gene Expression Assay. A total of 70,816 (CD11b^{+},CD11c^{+}) and 31,612 (CD31^{+}, PDPN^{+}, CD45$_{low}$) singlets were sorted for the control group. From the same sample preparation, 48,636 doublet (CD11b^{+}, CD11c^{+}, CD31^{+}, PDPN^{+}) events/cells were sorted provided to the Biotechnology Core for scRNA-seq. Both singlet and doublet tubes underwent treatment with 0.25 mg/mL Liberase TL (Roche) at 37*C on a shaker for 5

minutes. Samples were then washed and resuspended with a FACS buffer (1% BSA + 1x PBS). Cells were loaded onto a Chromium Controller to generate a single cell + barcoded gel-bead emulsion. Libraries were prepped with the 10X Genomics 3' reagents kit (v3 chemistry). The target recovery rate was 3,000 cells with a targeted read depth of 76,000 per cell. Cells were sequenced on the NovaSeq S1 100-cycle flow cell in collaboration with the University of Wisconsin Biotechnology Center (UWBC) DNA Sequencing Facility. Data were analyzed by the UW Bioinformatics Resource Center. Experimental data were demultiplexed using the Cell Ranger Single Cell Software Suite, mkfastq command wrapped around Illumina's bcl2fastq. The Miseq balancing run was quality controlled using calculations based on UMI tools (Smith et al., 2017). Sample libraries were balanced for the number of estimated reads per cell and run on an Illumina NovaSeq system. Cell Ranger software was then used to perform demultiplexing, alignment, filtering, barcode counting, UMI counting, and gene expression estimation for each sample according to the 10x Genomics documentation. Barcodes containing unusually high numbers of detected transcripts indicative of a doublet signature were excluded. The resulting data were then analyzed and explored using the Loupe Cell Browser software and the R packages clusterProlifer and/or monacle3 after excluding cells that made it through the FACS-enrichment. In total, 5115 (no-contact) and 4423 (post-contact) cells were identified in the analysis. 9,538 cells sequenced total (combined from no-contact and post-contact runs). Filtered cells for differential analysis using the following criteria: Cells have > 200 genes expressed, Cells have < 3,500 genes expressed, Cells have < 5% mitochondrial genes expressed. Using these criteria, filtered down to 4,132 cells for downstream analyses. 1,971 and 2,161 cells from no-contact run and post-contact run, respectively.

Gene ontologies and Ligand Receptor analysis

Genes identified to be differentially expressed from each cluster were separately assessed by gene ontological analyses using R package clusterProfiler (Yu et al., 2012). The genes that passed filtering during alignment were used as the background set during over-representation analyses. Significant gene ontological terms were identified using an adjusted P-value < 0.05. Bar plots, gene-concept network plots, and enrichment maps were visualized and generated using clusterProfiler. For receptor ligand interaction analysis we utilized TALKIEN: crossTALK IntEraction Network (Moratalla-Navarro et al., 2023). TALKIEN integrated analysis utilizes Ligand-Receptor DataBases from four sources: CellChat, CellPhoneDB, iCellNet, and Ramilowsky datasets (Moratalla-Navarro et al., 2023).

In vivo CD45 I.V. labeling

EAE was induced in C57BL/6 wild-type mice, and at peak disease score mice were intravenously (I.V.) injected with 2.5 µg of CD45 antibody conjugated to Alexa647 (Biolegend, Catalog #: 109818) in 200 µL of PBS as previously described (Anderson et al., 2014). 3 minutes before harvest to control for *ex vivo* unspecific binding of blood-derived cells to cribriform plate niche. Unperfused mice were used as positive controls to visualize blood-derived binding of leukocytes to cribriform plate niche, where intravenous delivery of CD45 antibody labeled at least 95% of blood-derived leukocytes after 3 minutes. Perfused mice were used for all experiments. Cribriform plates were then processed for flow as described previously, and processed using Cytek's 3-laser Northern Lights.

Statistics

When comparing results from two groups, unpaired Student's t-test was used. When comparing results from three groups, one-way ANOVA using Tukey's post-hoc multiple comparisons test was used. When comparing results across time, two-way ANOVA using Sidak's multiple comparisons test was used. All statistical analysis was performed using Graphpad Prism 6.0 software. Data is portrayed as the mean +/- standard error of the mean (S.E.M.), and significance portrayed as: n.s. = non-significant, $p > 0.05$; *$p < 0.05$; **$p < 0.01$; ***$p < 0.001$; ****$p < 0.0001$

Data availability

Single cell RNA sequence data was deposited at Array Express under the accession code E-MTAB-16132. (*https://www.ebi.ac.uk/biostudies/ArrayExpress/studies/E-MTAB-16132?key=ef1d4528-1084-4775-a5dc-2fb71d5a5e83*)

Supplemental figures

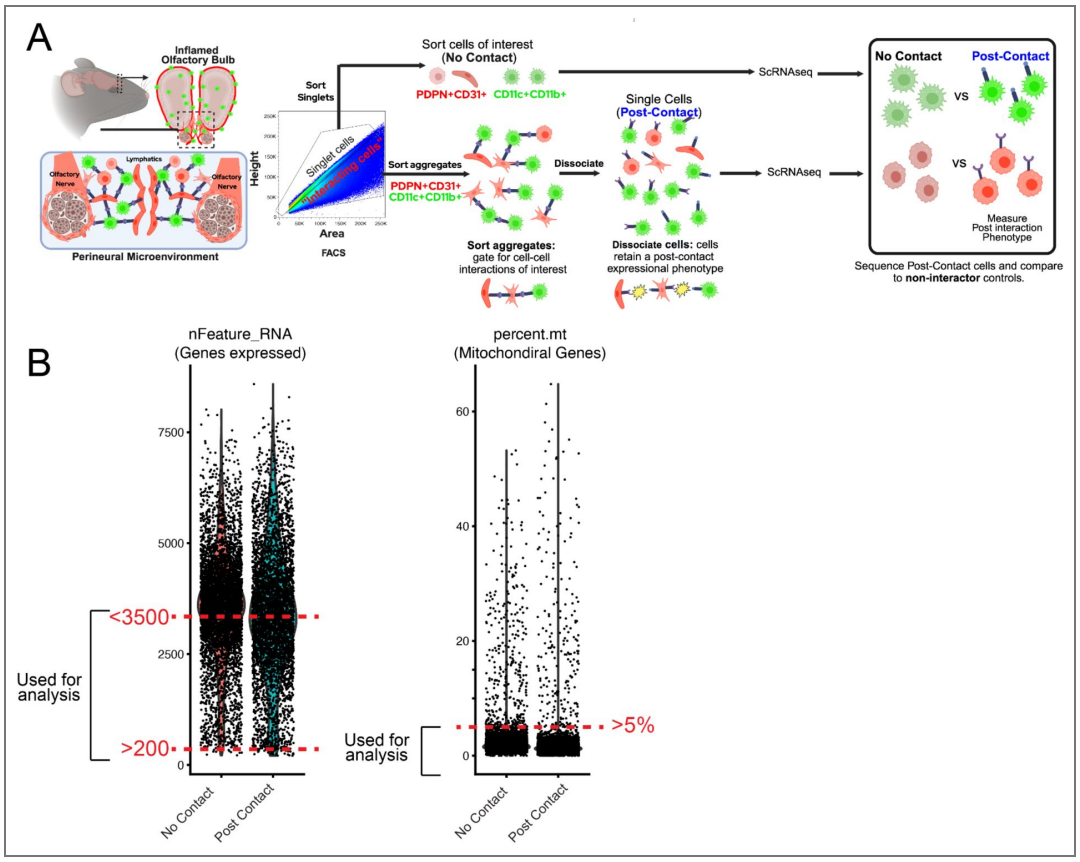

Supplemental Figure 1. Strategy to isolate CD11b+CD11c+PDPN+CD11b+ "No contact" and "Post-Contact" populations (A): Cartoon scheme outlining "PostContact-seq" sorting procedure of cribriform plate + Olfactory bulb tissue preparations from EAE 3.0. Sorted singlets from $CD11c^{+}CD11b^{+}$ (Myeloid cells) and $CD31^{+}PDPN^{+}$ (Meningeal-Lymphatic niche) gates were collected into a no-contact tube. Simultaneously, quadruple positive $CD11c^{+}CD11b^{+}CD31^{+}PDPN^{+}$ (Myeloid cell+Meningeal Lymphatic Niche) aggregating cells were sorted into the "interactor" tube. Prior to scRNAseq, both tubes underwent short liberase treatment to dissociate interacting cells and generate single cell suspensions of post-contact, and sequenced. **(B) :** Cutoffs for filtered cells for differential analysis using the following criteria: Cells have > 200 genes expressed, Cells have < 3,500 genes expressed, Cells have < 5% mitochondrial genes expressed. Strategy limits doublet aggregates at time of sequencing (High nFeatureRNA) and dead cells (High Percentage Mt).

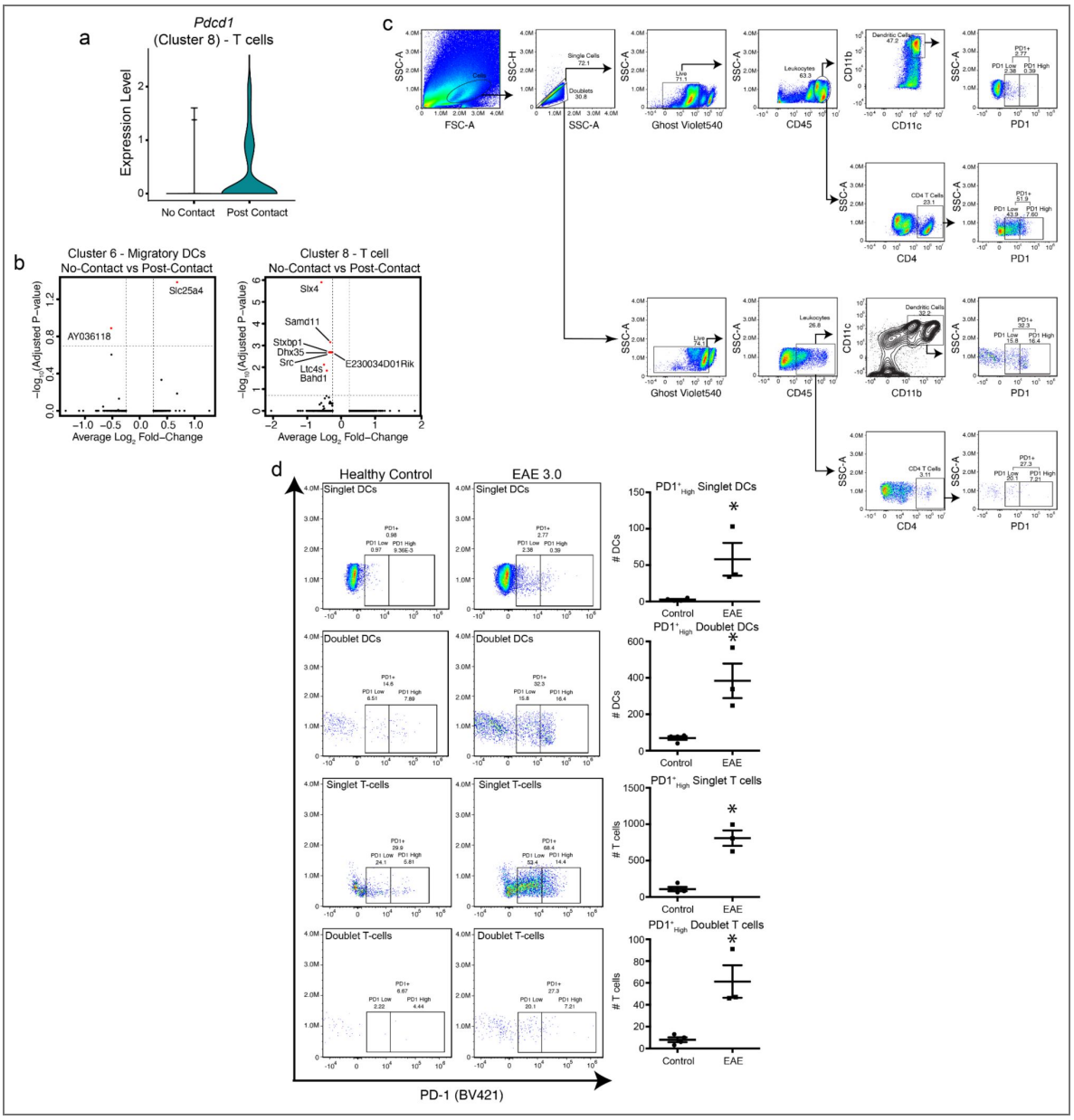

Supplemental Figure 2. Analysis of PD-1^{+} immune subsets in isolated cribriform plate cell suspensions

(A) Violin plot showing *Pdcd1* (PD-1) expression in T cells (Cluster 8) stratified by inferred cell-cell interactions, with higher expression observed in post contact T cells. **(B)** Volcano plots of differential gene expression between post-contact and no-contact cells in Cluster 6 migratory dendritic cells (left) and Cluster 8 T cells (right) **(C)** Flow cytometry gating strategy for identifying singlet and doublet populations of CD45^{+} leukocytes, dendritic cells (CD11c^{+}), and CD4^{+} T cells, followed by assessment of PD-1 expression across subsets. No liberase treatment given **(D)** Representative flow plots and quantification of PD-1^{high} singlet and doublet dendritic cells and T cells in healthy control and EAE day 3.0 mice. EAE mice show significantly elevated PD-1^{high} populations across all subsets, with the largest increase observed in doublet T cells, suggesting enhanced immune interaction and checkpoint activation during neuroinflammation. Singlet DCs (p=0.0322), Doublet DCs (p=0.0084), Singlet T cells (p=0.0005), Doublet T cells (p=0.0007). Unpaired two-tailed t test. Data are represented as mean ± SEM

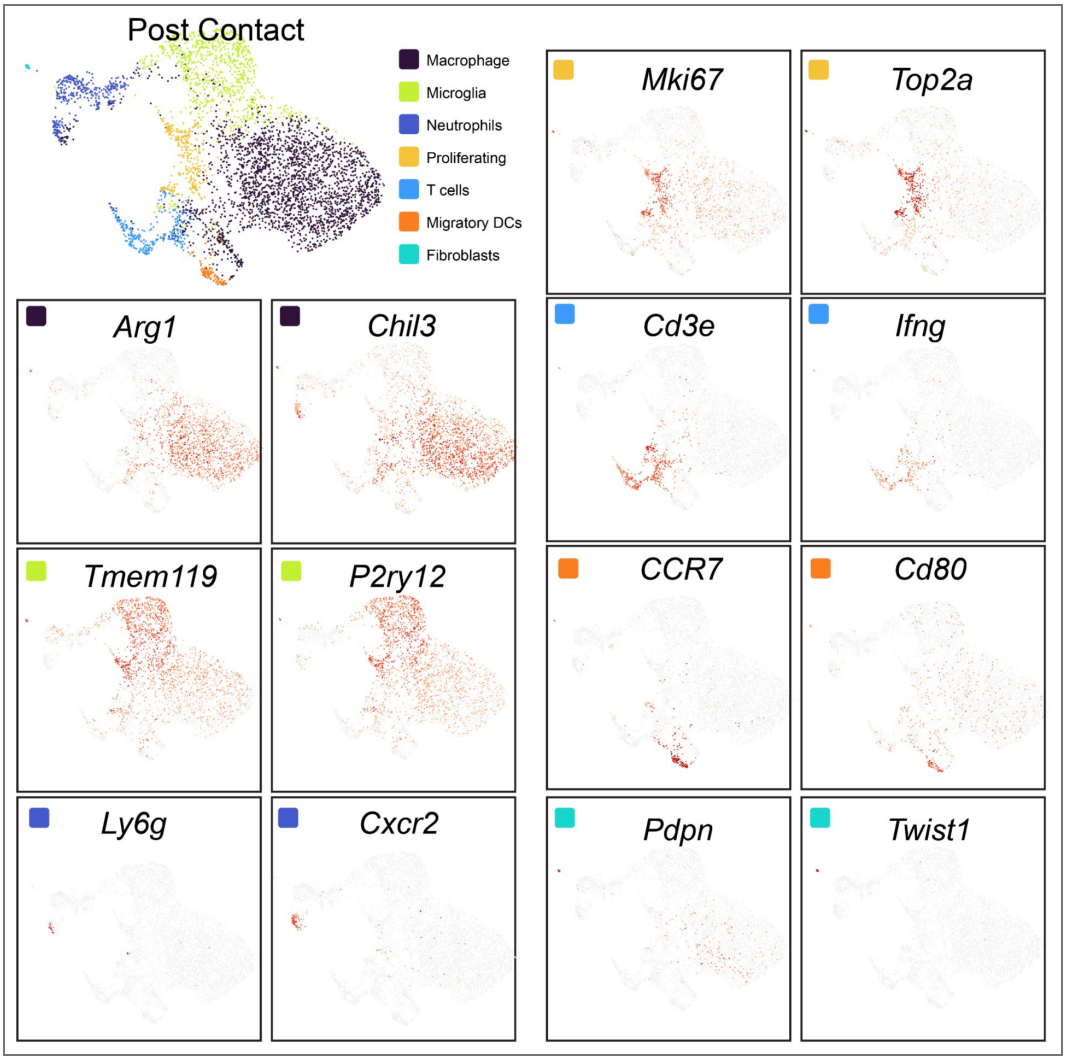

Supplemental Figure 3. Cell cluster characterization of "post contact" CD11b^{+}CD11c^{+} PDPN^{+}CD31^{+} interacting cells

UMAP projection (top left) shows major post contact cell types isolated, including macrophages (purple), microglia (green), neutrophils (blue), T cells (orange), proliferating cells (light blue), migratory dendritic cells (yellow-orange), and fibroblasts (aqua). Feature plots highlight expression of *Arg1*, *Ly6c2*, *Ccr2*, *Chil3* (CHI3L3), and *Pdpn*, identifying infiltrating monocyte-derived, alternatively activated macrophages, distinct from T cells (*Cd3e*, *Ifng*), DCs (*CCR7*, *Cd80*), microglia (*Tmem119*, *P2ry12*), neutrophils (*Ly6g*, *Cxcr2*), and proliferating cells (*Mki67*, *Top2a*). Gene ontology enrichment analysis (bottom) demonstrates that these post contact macrophages are enriched for pathways in Fcγ receptor and complement receptor signaling, negative regulation of IL-12 production, homotypic cell-cell adhesion, and hemostasis.

Supplemental Figure 4. Accumulation of CCR2$^+$ immune cells in PDPN$^+$ cribriform regions during EAE

(A) Immunofluorescence images of healthy and EAE 3.0 olfactory bulbs (OBs), showing increased CCR2$^+$ macrophage accumulation at the olfactory-cribriform junction. Insets show higher magnification of boxed areas with increased CCR2$^+$ cell localization to PDPN-rich regions in EAE. **(B)** Quantification of CCR2$^+$ cell numbers and their proportion in contact with PDPN-rich zones at the olfactory-cribriform interface. EAE mice show significantly more CCR2$^+$ cells and higher PDPN-association. Unpaired two-tailed t test. Data are represented as mean ± SEM (p = 0.0027). **(C)** High-magnification image showing CCR2$^+$ cells (green) embedded within cribriform plate lymphatic vessels (CPLVs, marked by LYVE-1, white) and adjacent to PDPN$^+$ region (red) at the olfactory nerve (ON) interface in EAE 3.0 mice. Arrowheads indicate CCR2$^+$ cells associated with CPLVs. Unpaired two-tailed t test. Data are represented as mean ± SEM (p = 0.0064)

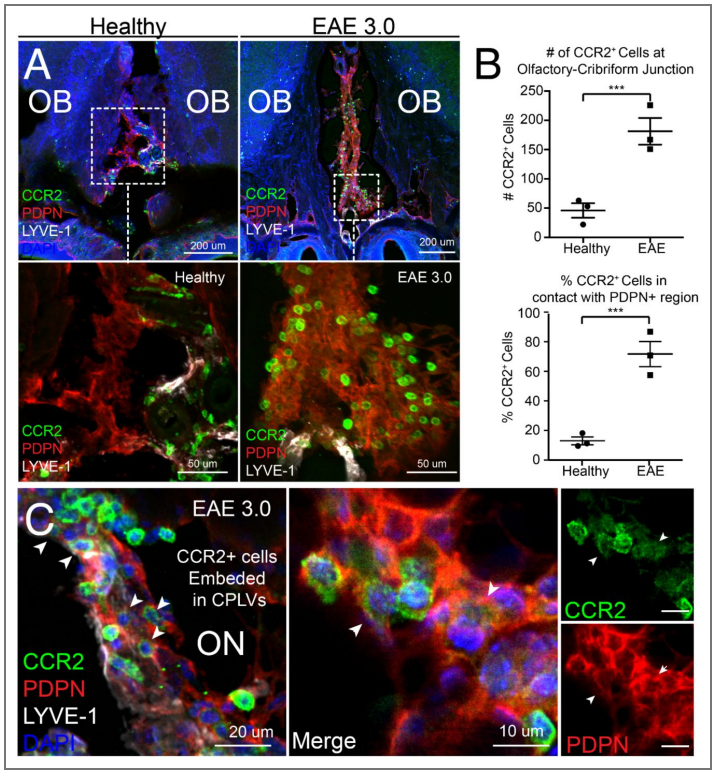

Supplemental Figure 5. Gating strategy for CD45-IV+ interactors

Isolation of specific cell populations, beginning with size-based selection (FSC-A/SSC-A) and doublet inclusion. The hierarchy branches to identify endothelial and stromal subsets (CD31/Podoplanin) while simultaneously profiling myeloid compartments through specific surface markers (CD11c/CD11b). Finally, the analysis incorporates intravascular cell labeling (CD45-IV) and viability dye (Ghost UV450-H) to precisely quantify live leukocyte populations within the sample.

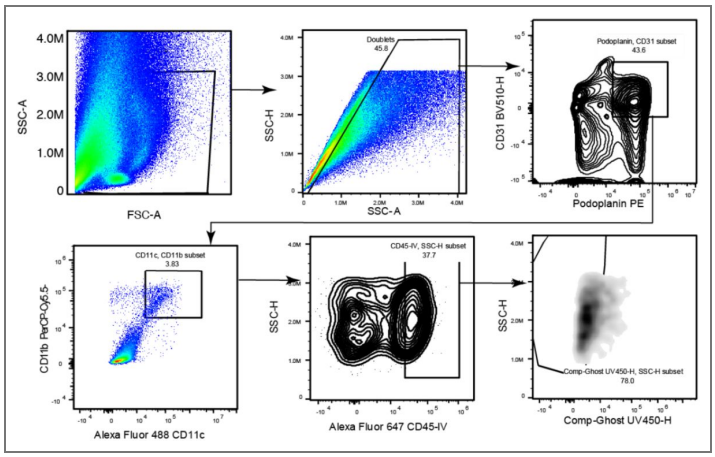

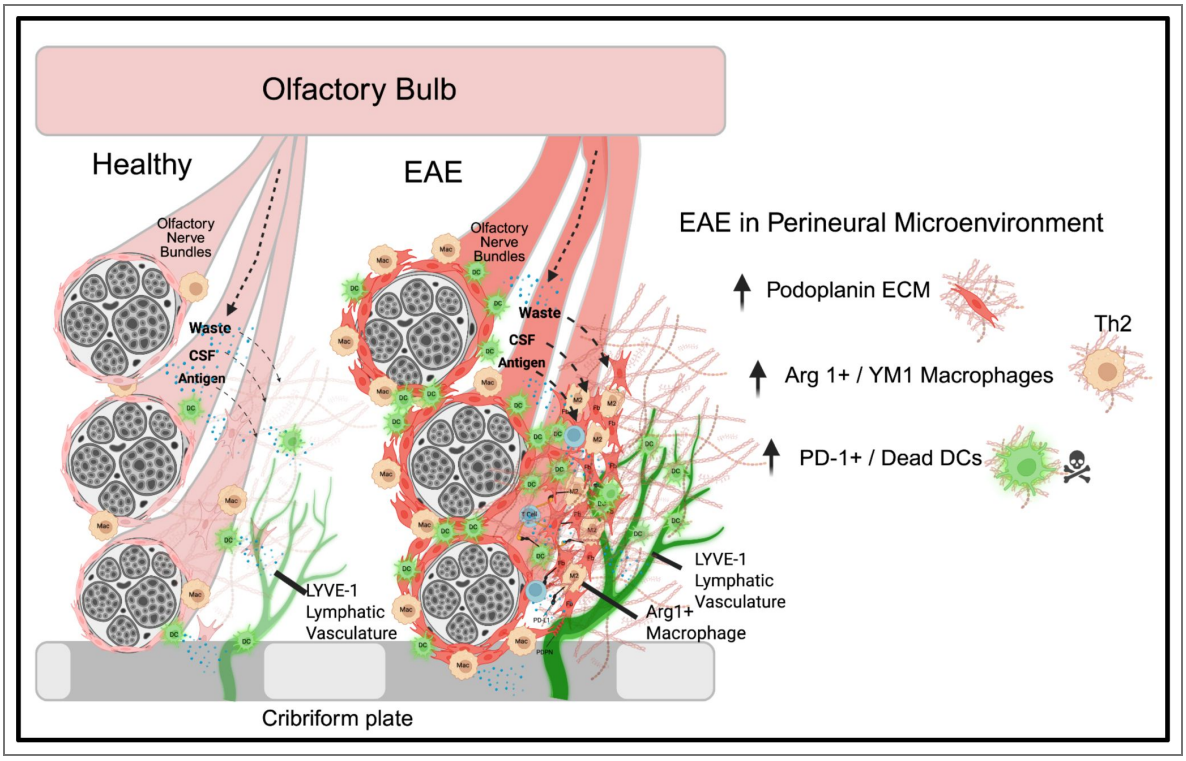

Supplemental Figure 6. Graphical Summary.

Perineural Microenvironment (PME) has Expanded Immune-Stromal-Lymphatic Niche During EAE. In the healthy state the PME of olfactory nerve bundles (ON) have lower levels of myeloid cells and lymphatics but still have access to draining cerebrospinal fluid (CSF), waste, antigen, and immune cells like DCs. During EAE neuroinflammation the PME becomes remodeled with higher myeloid cell accumulation within PDPN+ regions: fibroblasts, lymphatics, ECM, and macrophages. This creates an assembled immunoregulatory environment around olfactory nerve bundles where tolerogenic myeloid cells engage in cell-cell interactions alongside nerve bundles and cribriform lymphatics.

Additional information

Funding

This review is supported by the National Institutes of Health Grants NS126595 awarded to ZF. NS123449 awarded to MS. UW-Madison Neuroscience Training Program T32NS105602, AHA grant 915125, and Yi-ming and Hua-nien C. Yin Fellowship awarded to CL. UW-Madison Cellular, Molecular, and Pathology Training Program T32GM135119 awarded to JP and SV. UW-Madison Medical Scientist Training Program T32GM140935 awarded to SV.

Funding

Funder	Grant reference number	Author
National Institute of Neurological Disorders and Stroke (NINDS)	NS126595	Zsuzsanna Fabry
National Institute of Neurological Disorders and Stroke (NINDS)	NS123449	Matyas Sandor
National Institute of Neurological Disorders and Stroke (NINDS)	T32NS105602	Collin Laaker
American Heart Association (AHA)	915125	Collin Laaker
National Institute of General Medical Sciences (NIGMS)	T32GM135119	Jenna Port Sophia M Vrba
National Institute of General Medical Sciences (NIGMS)	T32GM140935	Sophia M Vrba

Author ORCID iDs

Collin Laaker: https://orcid.org/0000-0001-8532-9427
Zsuzsanna Fabry: https://orcid.org/0000-0003-4555-9732

References

Anderson K.G., Mayer-Barber K., Sung H., Beura L., James B.R., Taylor J.J., Qunaj L., Griffith T.S., Vezys V., Barber D.L., *et al.* (2014) Intravascular staining for discrimination of vascular and tissue leukocytes. *Nat Protoc* **9**:209-222 https://doi.org/10.1038/nprot.2014.005 | PubMed

Baruch E.N., Gleber-Netto F.O., Nagarajan P., Rao X., Akhter S., Eichwald T., Xie T., Balood M., Adewale A., Naara S., *et al.* (2025) Cancer-induced nerve injury promotes resistance to anti-PD-1 therapy. *Nature* 1-12 https://doi.org/10.1038/s41586-025-09370-8 | PubMed

Bendall S.C (2020) Diamonds in the doublets. *Nat Biotechnol* **38**:559-561 https://doi.org/10.1038/s41587-020-0511-6 | PubMed

Bieniasz-Krzywiec P., Martín-Pérez R., Ehling M., García-Caballero M., Pinioti S., Pretto S., Kroes R., Aldeni C., Di Matteo M., Prenen H., *et al.* (2019) Podoplanin-Expressing Macrophages Promote Lymphangiogenesis and Lymphoinvasion in Breast Cancer. *Cell Metab* **30**:917-936. https://doi.org/10.1016/j.cmet.2019.07.015 | PubMed

Çavdar S., Altınöz D., Dilan D.T., İ A.G., Özcan G. (2024) Extracranial transport of brain lymphatics via cranial nerve in human. *Neuroscience letters* **827** https://doi.org/10.1016/j.neulet.2024.137737 | PubMed

Chen S.-H., Zhang B.-Y., Zhou B., Zhu C.-Z., Sun L.-Q., Feng Y.-J. (2019) Perineural invasion of cancer: a complex crosstalk between cells and molecules in the perineural niche. *American Journal of Cancer Research* **9**:1 PubMed

Choi Y.H., Hsu M., Laaker C., Port J., Kovács K.G., Herbath M., Yang H., Cismaru P., Johnson A.M., Spellman B., *et al.* (2025) Dual role of vascular endothelial growth factor-C in post-stroke recovery. *J Exp Med* **222** https://doi.org/10.1084/jem.20231816 | PubMed

Clarkson B.D., Walker A., Harris M.G., Rayasam A., Hsu M., Sandor M., Fabry Z. (2017) CCR7 deficient inflammatory Dendritic Cells are retained in the Central Nervous System. *Sci Rep* **7**:42856 https://doi.org/10.1038/srep42856 | PubMed

Clarkson B.D., Walker A., Harris M.G., Rayasam A., Sandor M., Fabry Z. (2015) CCR2-dependent dendritic cell accumulation in the central nervous system during early effector experimental autoimmune encephalomyelitis is essential for effector T cell restimulation in situ and disease progression. *J Immunol* **194**:531-541 https://doi.org/10.4049/jimmunol.1401320 | PubMed

Da Mesquita S., Louveau A., Vaccari A., Smirnov I., Cornelison R.C., Kingsmore K.M., Contarino C., Onengut-Gumuscu S., Farber E., Raper D., *et al.* (2018) Functional aspects of meningeal lymphatics in ageing and Alzheimer's disease. *Nature* **560**:185-191 https://doi.org/10.1038/s41586-018-0368-8 | PubMed

Decker Y., Krämer J., Xin L., Müller A., Scheller A., Fassbender K., Proulx S.T. (2022) Magnetic resonance imaging of cerebrospinal fluid outflow after low-rate lateral ventricle infusion in mice. *JCI Insight* **7** https://doi.org/10.1172/jci.insight.150881 | PubMed

Dorrier C.E., Jones H.E., Pintarić L., Siegenthaler J.A., Daneman R. (2022) Emerging roles for CNS fibroblasts in health, injury and disease. *Nat Rev Neurosci* **23**:23-34 https://doi.org/10.1038/s41583-021-00525-w | PubMed

Fahmy L.M., Chen Y., Xuan S., Haacke E.M., Hu J., Jiang Q. (2021) All Central Nervous System Neuro- and Vascular-Communication Channels Are Surrounded With Cerebrospinal Fluid. *Front Neurol* **12**:614636 https://doi.org/10.3389/fneur.2021.614636 | PubMed

Fitzpatrick Z., Ghabdan Zanluqui N., Rosenblum J.S., Tuong Z.K., Lee C.Y.C., Chandrashekhar V., Negro-Demontel M.L., Stewart A.P., Posner D.A., Buckley M., *et al.* (2024) Venous-plexus-associated lymphoid hubs support meningeal humoral immunity. *Nature* **628**:612-619 https://doi.org/10.1038/s41586-024-07202-9 | PubMed

Giladi A., Cohen M., Medaglia C., Baran Y., Li B., Zada M., Bost P., Blecher-Gonen R., Salame T.M., Mayer J.U., *et al.* (2020) Dissecting cellular crosstalk by sequencing physically interacting cells. *Nature biotechnology* **38** https://doi.org/10.1038/s41587-020-0442-2 | PubMed

Ginhoux F., Guilliams M., Merad M. (2022) Expanding dendritic cell nomenclature in the single-cell era. *Nat Rev Immunol* **22**:67-68 https://doi.org/10.1038/s41577-022-00675-7 | PubMed

Gordon S.R., Maute R.L., Dulken B.W., Hutter G., George B.M., McCracken M.N., Gupta R., Tsai J.M., Sinha R., Corey D., *et al.* (2017) PD-1 expression by tumour-associated macrophages inhibits phagocytosis and tumour immunity. *Nature* **545**:495-499 https://doi.org/10.1038/nature22396 | PubMed

Herz J., Louveau A., Da Mesquita S., Kipnis J. (2018) Morphological and Functional Analysis of CNS-Associated Lymphatics. *Methods Mol Biol* **1846**:141-151 https://doi.org/10.1007/978-1-4939-8712-2_9 | PubMed

Hitpass Romero K., Stevenson T.J., Smyth L.C.D., Watkin B., McCullough S.J.C., Vinnell L., Smith A.M., Schweder P., Correia J.A., Kipnis J., *et al.* (2025) Age-related meningeal extracellular matrix remodeling compromises CNS lymphatic function. *J Neuroinflammation* **22**:109 https://doi.org/10.1186/s12974-025-03436-0 | PubMed

Hsu M., Laaker C., Madrid A., Herbath M., Choi Y.H., Sandor M., Fabry Z. (2022) Neuroinflammation creates an immune regulatory niche at the meningeal lymphatic vasculature near the cribriform plate. *Nat Immunol* **23**:581-593 https://doi.org/10.1038/s41590-022-01158-6 | PubMed

Hsu M., Rayasam A., Kijak J.A., Choi Y.H., Harding J.S., Marcus S.A., Karpus W.J., Sandor M., Fabry Z. (2019) Neuroinflammation-induced lymphangiogenesis near the cribriform plate contributes to drainage of CNS-derived antigens and immune cells. *Nat Commun* **10**:1-14 https://doi.org/10.1038/s41467-018-08163-0 | PubMed

Hu X., Deng Q., Ma L., Li Q., Chen Y., Liao Y., Zhou F., Zhang C., Shao L., Feng J., *et al.* (2020) Meningeal lymphatic vessels regulate brain tumor drainage and immunity. *Cell Res* **30**:229-243 https://doi.org/10.1038/s41422-020-0287-8 | PubMed

Jiang Z., Jiang J.X., Zhang G.-X. (2014) Macrophages: a double-edged sword in experimental autoimmune encephalomyelitis. *Immunol Lett* **160**:17-22 https://doi.org/10.1016/j.imlet.2014.03.006 | PubMed

Jin H., Yoon J.-H., Hong S.P., Hwang Y.S., Yang M.J., Choi J., Kang H.J., Baek S.E., Jin C., Jung J., *et al.* (2025) Increased CSF drainage by non-invasive manipulation of cervical lymphatics. *Nature* 1-13 https://doi.org/10.1038/s41586-025-09052-5 | PubMed

Jordão MJC, Sankowski R, Brendecke SM, Sagar, Locatelli G, Tai YH, Tay TL, Schramm E, Armbruster S, Hagemeyer N, *et al.* (2019) Single-cell profiling identifies myeloid cell subsets with distinct fates during neuroinflammation. *Science* **363** https://doi.org/10.1126/science.aat7554 | PubMed

Karman J., Ling C., Sandor M., Fabry Z. (2004) Initiation of immune responses in brain is promoted by local dendritic cells. *J Immunol* **173**:2353-2361 https://doi.org/10.4049/jimmunol.173.4.2353 | PubMed

Karyampudi L., Lamichhane P., Krempski J., Kalli K.R., Behrens M.D., Vargas D.M., Hartmann L.C., Janco J.M.T., Dong H., Hedin K.E., *et al.* (2016) PD-1 Blunts the Function of Ovarian Tumor-Infiltrating Dendritic Cells by Inactivating NF-κB. *Cancer Res* **76**:239-250 https://doi.org/10.1158/0008-5472.can-15-0748 | PubMed

Keren-Shaul H., Spinrad A., Weiner A., Matcovitch-Natan O., Dvir-Szternfeld R., Ulland T.K., David E., Baruch K., Lara-Astaiso D., Toth B., *et al.* (2017) A Unique Microglia Type Associated with Restricting Development of Alzheimer's Disease. *Cell* **169**:1276-1290. https://doi.org/10.1016/j.cell.2017.05.018 | PubMed

Kipnis J (2024) The anatomy of brainwashing. *Science* https://doi.org/10.1126/science.adp1705 | PubMed

Klement J.D., Redd P.S., Lu C., Merting A.D., Poschel D.B., Yang D., Savage N.M., Zhou G., Munn D.H., Fallon P.G., *et al.* (2023) Tumor PD-L1 engages myeloid PD-1 to suppress type I interferon to impair cytotoxic T lymphocyte recruitment. *Cancer Cell* **41**:620-636. https://doi.org/10.1016/j.ccell.2023.02.005 | PubMed

Knutson K.L (2024) Regulation of Tumor Dendritic Cells by Programmed Cell Death 1 Pathways. *J Immunol* **212**:1397-1405 https://doi.org/10.4049/jimmunol.2300674 | PubMed

Krempski J., Karyampudi L., Behrens M.D., Erskine C.L., Hartmann L., Dong H., Goode E.L., Kalli K.R., Knutson K.L. (2011) Tumor-infiltrating programmed death receptor-1+ dendritic cells mediate immune suppression in ovarian cancer. *J Immunol* **186**:6905-6913 https://doi.org/10.4049/jimmunol.1100274 | PubMed

Kwiecień I., Rutkowska E., Raniszewska A., Sokołowski R., Bednarek J., Jahnz-Różyk K., Rzepecki P., Domagała-Kulawik J. (2022) Immunosuppressive properties of human PD-1 +, PDL-1 + and CD80 + dendritic cells from lymph nodes aspirates of lung cancer patients. *Cancer Immunol Immunother* https://doi.org/10.1007/s00262-022-03178-5 | PubMed

Laaker C., Baenen C., Kovács K.G., Sandor M., Fabry Z. (2023) Immune cells as messengers from the CNS to the periphery: the role of the meningeal lymphatic system in immune cell migration from the CNS. *Front Immunol* **14**:1233908 https://doi.org/10.3389/fimmu.2023.1233908 | PubMed

Laaker C.J., Kovacs K.G., Baenen C.M., Hsu M., Port J.M., Vrba S.M., Kumar M., Hubacek A.J., Herbath M., Priyathilaka T.T., *et al.* (2025) Perineural immune environment of olfactory nerves is reshaped by neuroinflammatory drainage and connects to ethmoid bone marrow. *Sci Adv* **11**:eadt9591 https://doi.org/10.1126/sciadv.adt9591 | PubMed

Lamichhane P., Karyampudi L., Shreeder B., Krempski J., Bahr D., Daum J., Kalli K.R., Goode E.L., Block M.S., Cannon M.J., *et al.* (2017) IL10 Release upon PD-1 Blockade Sustains Immunosuppression in Ovarian Cancer. *Cancer Res* **77**:6667-6678 https://doi.org/10.1158/0008-5472.can-17-0740 | PubMed

Liebig C., Ayala G., Wilks J.A., Berger D.H., Albo D. (2009) Perineural invasion in cancer. *Cancer* **115**:3379-3391 https://doi.org/10.1002/cncr.24396 | PubMed

Lim T.S., Chew V., Sieow J.L., Goh S., Yeong J.P.-S., Soon A.L., Ricciardi-Castagnoli P. (2016) PD-1 expression on dendritic cells suppresses CD8+ T cell function and antitumor immunity. *Oncoimmunology* **5**:e1085146 https://doi.org/10.1080/2162402x.2015.1085146 | PubMed

Li T., Wang X., Niu M., Wang M., Zhou J., Wu K., Yi M. (2023) Bispecific antibody targeting TGF-β and PD-L1 for synergistic cancer immunotherapy. *Front Immunol* **14**:1196970 https://doi.org/10.3389/fimmu.2023.1196970 | PubMed

Louveau A., Herz J., Alme M.N., Salvador A.F., Dong M.Q., Viar K.E., Herod S.G., Knopp J., Setliff J.C., Lupi A.L., *et al.* (2018) CNS lymphatic drainage and neuroinflammation are regulated by meningeal lymphatic vasculature. *Nat Neurosci* **21**:1380-1391 https://doi.org/10.1038/s41593-018-0227-9 | PubMed

Louveau A., Smirnov I., Keyes T.J., Eccles J.D., Rouhani S.J., David Peske J., Derecki N.C., Castle D., Mandell J.W., Lee K.S., *et al.* (2015) Structural and functional features of central nervous system lymphatic vessels. *Nature* **523**:337-341 https://doi.org/10.1038/nature14432 | PubMed

Maier B., Leader A.M., Chen S.T., Tung N., Chang C., LeBerichel J., Chudnovskiy A., Maskey S., Walker L., Finnigan J.P., *et al.* (2020) A conserved dendritic-cell regulatory program limits antitumour immunity. *Nature* **580**:257-262 https://doi.org/10.1038/s41586-020-2134-y | PubMed

Mohammad M.G., Tsai V.W.W., Ruitenberg M.J., Hassanpour M., Li H., Hart P.H., Breit S.N., Sawchenko P.E., Brown D.A. (2014) Immune cell trafficking from the brain maintains CNS immune tolerance. *J Clin Invest* **124**:1228-1241 https://doi.org/10.1172/jci71544 | PubMed

Møllgård K., Beinlich F.R.M., Kusk P., Miyakoshi L.M., Delle C., Plá V., Hauglund N.L., Esmail T., Rasmussen M.K., Gomolka R.S., *et al.* (2023) A mesothelium divides the subarachnoid space into functional compartments. *Science* **379**:84-88 https://doi.org/10.1126/science.adc8810 | PubMed

Mondanelli G., Bianchi R., Pallotta M.T., Orabona C., Albini E., Iacono A., Belladonna M.L., Vacca C., Fallarino F., Macchiarulo A., *et al.* (2017) A Relay Pathway between Arginine and Tryptophan Metabolism Confers Immunosuppressive Properties on Dendritic Cells. *Immunity* **46**:233-244 https://doi.org/10.1016/j.immuni.2017.01.005 | PubMed

Moratalla-Navarro F., Moreno V., Sanz-Pamplona R. (2023) TALKIEN: crossTALK IntEraction Network. A web-based tool for deciphering molecular communication through ligand-receptor interactions. *Molecular omics* **19** https://doi.org/10.1039/d3mo00049d | PubMed

Mrdjen D., Pavlovic A., Hartmann F.J., Schreiner B., Utz S.G., Leung B.P., Lelios I., Heppner F.L., Kipnis J., Merkler D., *et al.* (2018) High-Dimensional Single-Cell Mapping of Central Nervous System Immune Cells Reveals Distinct Myeloid Subsets in Health, Aging, and Disease. *Immunity* **48**:380-395. https://doi.org/10.1016/j.immuni.2018.01.011 | PubMed

Murray P.J (2017) Macrophage Polarization. *Annu Rev Physiol* **79**:541-566 https://doi.org/10.1146/annurev-physiol-022516-034339 | PubMed

Park S.J., Namkoong H., Doh J., Choi J.-C., Yang B.-G., Park Y., Chul Sung Y. (2014) Negative role of inducible PD-1 on survival of activated dendritic cells. *J Leukoc Biol* **95**:621-629 https://doi.org/10.1189/jlb.0813443 | PubMed

Proulx S.T (2021) Cerebrospinal fluid outflow: a review of the historical and contemporary evidence for arachnoid villi, perineural routes, and dural lymphatics. *Cell Mol Life Sci* **78**:2429-2457 https://doi.org/10.1007/s00018-020-03706-5 | PubMed

Reichardt W., Dürr C., von Elverfeldt D., Jüttner E., Gerlach U.V., Yamada M., Smith B., Negrin R.S., Zeiser R. (2008) Impact of mammalian target of rapamycin inhibition on lymphoid homing and tolerogenic function of nanoparticle-labeled dendritic cells following allogeneic hematopoietic cell transplantation. *J Immunol* **181**:4770-4779 https://doi.org/10.4049/jimmunol.181.7.4770 | PubMed

Rustenhoven J., Drieu A., Mamuladze T., de Lima K.A., Dykstra T., Wall M., Papadopoulos Z., Kanamori M., Salvador A.F., Baker W., *et al.* (2021) Functional characterization of the dural sinuses as a neuroimmune interface. *Cell* **184**:1000-1016. https://doi.org/10.1016/j.cell.2020.12.040 | PubMed

Schreiner B., Bailey S.L., Shin T., Chen L., Miller S.D. (2008) PD-1 ligands expressed on myeloid-derived APC in the CNS regulate T-cell responses in EAE. *European Journal of Immunology* **38**:2706-2717 https://doi.org/10.1002/eji.200838137 | PubMed

Smith T., Heger A., Sudbery I. (2017) UMI-tools: modeling sequencing errors in Unique Molecular Identifiers to improve quantification accuracy. *Genome Research* **27**:491-499 https://doi.org/10.1101/gr.209601.116 | PubMed

Snyder J.P., Amiel E. (2018) Regulation of Dendritic Cell Immune Function and Metabolism by Cellular Nutrient Sensor Mammalian Target of Rapamycin (mTOR). *Front Immunol* **9**:3145 https://doi.org/10.3389/fimmu.2018.03145 | PubMed

Spera I., Cousin N., Ries M., Kedracka A., Castillo A., Aleandri S., Vladymyrov M., Mapunda J.A., Engelhardt B., Luciani P., *et al.* (2023) Open pathways for cerebrospinal fluid outflow at the cribriform plate along the olfactory nerves. *EBioMedicine* **91**:104558 https://doi.org/10.1016/j.ebiom.2023.104558 | PubMed

Strauss L., Mahmoud M.A.A., Weaver J.D., Tijaro-Ovalle N.M., Christofides A., Wang Q., Pal R., Yuan M., Asara J., Patsoukis N., *et al.* (2020) Targeted deletion of PD-1 in myeloid cells induces antitumor immunity. *Sci Immunol* **5** https://doi.org/10.1126/sciimmunol.aay1863 | PubMed

Sukhbaatar N., Hengstschläger M., Weichhart T. (2016) mTOR-Mediated Regulation of Dendritic Cell Differentiation and Function. *Trends Immunol* **37**:778-789 https://doi.org/10.1016/j.it.2016.08.009 | PubMed

Swartz M.A., Lund A.W. (2012) Lymphatic and interstitial flow in the tumour microenvironment: linking mechanobiology with immunity. *Nat Rev Cancer* **12**:210-219 https://doi.org/10.1038/nrc3186 | PubMed

Turnquist H.R., Raimondi G., Zahorchak A.F., Fischer R.T., Wang Z., Thomson A.W. (2007) Rapamycin-conditioned dendritic cells are poor stimulators of allogeneic CD4+ T cells, but enrich for antigen-specific Foxp3+ T regulatory cells and promote organ transplant tolerance. *J Immunol* **178**:7018-7031 https://doi.org/10.4049/jimmunol.178.11.7018 | PubMed

Wang P.L., Yim A.K.Y., Kim K.-W., Avey D., Czepielewski R.S., Colonna M., Milbrandt J., Randolph G.J. (2020) Peripheral nerve resident macrophages share tissue-specific programming and features of activated microglia. *Nat Commun* **11**:2552 https://doi.org/10.1038/s41467-020-16355-w | PubMed

Wang X., Wang X., Li J., Liang J., Ren X., Yun D., Liu J., Fan J., Zhang Y., Zhang J., *et al.* (2022a) PDPN contributes to constructing immunosuppressive microenvironment in IDH wildtype glioma. *Cancer Gene Therapy* **30**:345-357 https://doi.org/10.1038/s41417-022-00550-6 | PubMed

Wang Y.-M., Qiu J.-J., Qu X.-Y., Peng J., Lu C., Zhang M., Zhang M.-X., Qi X.-L., Lv B., Guo J.-J., *et al.* (2022b) Accumulation of dysfunctional tumor-infiltrating PD-1+ DCs links PD-1/PD-L1 blockade immunotherapeutic response in cervical cancer. *Oncoimmunology* **11**:2034257 https://doi.org/10.1080/2162402x.2022.2034257 | PubMed

Wlodarczyk A., Løbner M., Cédile O., Owens T. (2014) Comparison of microglia and infiltrating CD11c+ cells as antigen presenting cells for T cell proliferation and cytokine response. *Journal of Neuroinflammation* **11**:1-9 https://doi.org/10.1186/1742-2094-11-57 | PubMed

Wu M., Shi Y., Liu Y., Huang H., Che J., Shi J., Xu C. (2024) Exosome-transmitted podoplanin promotes tumor-associated macrophage-mediated immune tolerance in glioblastoma. *CNS Neuroscience & Therapeutics* **30**:e14643 https://doi.org/10.1111/cns.14643 | PubMed

Xiao Z., Wang R., Wang X., Yang H., Dong J., He X., Yang Y., Guo J., Cui J., Zhou Z. (2023) Impaired function of dendritic cells within the tumor microenvironment. *Front Immunol* **14**:1213629 https://doi.org/10.3389/fimmu.2023.1213629 | PubMed

Xin L., Madarasz A., Ivan D.C., Weber F., Aleandri S., Luciani P., Locatelli G., Proulx S.T. (2024) Impairment of spinal CSF flow precedes immune cell infiltration in an active EAE model. *J Neuroinflammation* **21**:272 https://doi.org/10.1186/s12974-024-03247-9 | PubMed

Xin L., Nishihara H., Madarasz A., Pleskac P., Tran L., Ivan D.C., Shimizu F., Aleandri S., Locatelli G., Luciani P., *et al.* (2025) Role of CSF flow and meningeal barriers in the development of inflammatory lesions at the CNS-PNS transition zone of cranial nerves in autoimmune demyelinating diseases. *Acta Neuropathol* **149**:65 https://doi.org/10.1007/s00401-025-02896-1 | PubMed

Ydens E., Amann L., Asselbergh B., Scott C.L., Martens L., Sichien D., Mossad O., Blank T., De Prijck S., Low D., *et al.* (2020) Profiling peripheral nerve macrophages reveals two macrophage subsets with distinct localization, transcriptome and response to injury. *Nature Neuroscience* **23**:676-689 https://doi.org/10.1038/s41593-020-0618-6 | PubMed

Yoon J.-H., Jin H., Kim H.J., Hong S.P., Yang M.J., Ahn J.H., Kim Y.-C., Seo J., Lee Y., McDonald D.M., *et al.* (2024) Nasopharyngeal lymphatic plexus is a hub for cerebrospinal fluid drainage. *Nature* **625**:768-777 https://doi.org/10.1038/s41586-023-06899-4 | PubMed

Yu G., Wang L.-G., Han Y., He Q.-Y. (2012) clusterProfiler: an R Package for Comparing Biological Themes Among Gene Clusters. *OMICS: A Journal of Integrative Biology* **16**:284-287 https://doi.org/10.1089/omi.2011.0118 | PubMed

Zhang P., Wang X., Yang X., Liu H. (2025a) Molecular control of PDPNhi macrophage subset induction by ADAP as a host defense in sepsis. *JCI Insight* **10** https://doi.org/10.1172/jci.insight.186456 | PubMed

Zhang Q., Niu Y., Li Y., Xia C., Chen Z., Chen Y., Feng H. (2025b) Meningeal lymphatic drainage: novel insights into central nervous system disease. *Signal Transduct Target Ther* **10**:142 https://doi.org/10.1038/s41392-025-02177-z | PubMed

Laaker CJ, Hsu M, Madrid A, Port J, Vrba SM, Herbath M, Baenen C, Kumar M, Priyathilaka TT, Sandor M, *et al.* (2025) Perineural Microenvironment at the Cribriform Plate Lymphatics Assembles a Suppressive Myeloid Network during EAE-induced Neuroinflammation. EMBL-EBI BioStudies. ID E-MTAB-16132 https://www.ebi.ac.uk/biostudies/ArrayExpress/studies/E-MTAB-16132

Peer reviews

Reviewer #1 (Public review):

Summary:

Laaker et al. investigates the immunological role of the cribriform plate during neuroinflammation using the EAE model. The authors combine immunohistochemistry, flow cytometry and single-cell RNA sequencing to characterize CD11b+CD11c+ myeloid cells that accumulate at podoplanin (PDPN)-rich meningeal-lymphatic niches surrounding olfactory nerve bundles. They identified distinct populations of migratory dendritic cells (DCs) and macrophages retained at the cribriform plate that exhibit transcriptional signatures consistent with immune tolerance, reduced interferon signaling, and programmed cell death, including Pdcd1 (PD-1) expression. In parallel, CCR2+ monocytes and alternatively activated (M2-like) Arg1+/CHI3L3+ macrophages integrate into this niche, suggesting the establishment of a locally immunosuppressive myeloid network.

Strengths:

(1) Overall, the study postulates a novel model in which the cribriform plate functions as a specialized perineural immune interface that reshapes myeloid phenotypes during neuroinflammation.

(2) Suggests broader relevance for shaping peripheral immunity and therapeutic targeting. If DCs are being "tuned" at this exit site, it could influence what reaches cervical lymph nodes and how peripheral responses are set during CNS autoimmunity; the authors explicitly position this as relevant to CNS autoimmunity and possibly other CNS diseases (while acknowledging the need for human validation).

(3) Technical sound and highly original work. Convergent multi-method support: the central narrative is backed by immunohistochemistry + flow cytometry + scRNA-seq, rather than a single assay. The headline conclusion (tolerogenic/suppressive skew at the cribriform plate during EAE) is explicitly built from these combined modalities.

Comments on revised version.

All my points were adequately addressed by the authors.

https://doi.org/10.7554/eLife.110460.2.sa2

Reviewer #2 (Public review):

Summary:

In this article, Laaker et al described diverse populations of macrophages and dendritic cells found in and around the cribriform plate in a context of a neuroinflammation caused by an autoimmune disease (EAE). The authors utilize elegant histochemical staining and a nifty approach to sort doublets to interrogate cells that are in contact with one another, presumably in vivo. Notably, they uncover a population of CD11c+CD11b+ cells interacting with M2 macrophages and PDPN+ fibroblasts and lymphatics. These cells are heterogenous but some of these DCs express PD-1 and transcriptional profiling suggests they may have immunosuppressive behavior. Altogether, this article explains well the complexity of cell populations found around the cribriform plate during inflammation and are suggestive of different interactions that trigger these different phenotypes from immune cells.

Strengths:

Beautiful images of a unique CNS: peripheral interface that support a novel scRNA approach to understanding how different cell populations engage in functional interactions in vivo.

Weaknesses:

It is unclear how the sorted populations reflect in vivo interactions, or a propensity to form aggregates during ex vivo processing. Future work will be needed to address which poplanin expressing cells are most relevant.

https://doi.org/10.7554/eLife.110460.2.sa1

Author response:

The following is the authors' response to the original reviews.

> ***Reviewer #1 (Public review):***
>
> *(1) (Figure 1): Quantification of CSF1R-GFP$^+$ and CD11c-eYFP$^+$ cells in PDPN$^+$LYVE-1$^-$ vs. PDPN$^+$LYVE-1$^+$ regions. "This would demonstrate selective accumulation or retention of myeloid cells at the cribriform plate niche."*

We thank the reviewer for this important suggestion. The representative images in Figure 1(Bottom) establish the partial justification for the cell sorting and sequencing strategy in Figure 3, which relies heavily on myeloid cells in contact with PDPN. Importantly, our previous publication Hsu et al. 2022 has quantified elevated Cd11c+ cells in contact with the Cribriform lymphatic niche. Figure 1 in this context seeks to show PDPN as an additional and broader marker for the meningeal and lymphatic tissue at the brain's border. Because PDPN represents more surface area, PDPN+Lyve-1- regions would likely show more immune cell accumulation but our primary argument is simply that myeloid cells also accumulate in both

PDPN regions. As a result we argue the quantification of cells in Lyve-1+ and negative regions is not necessary. We have added a sentence to the text which explains the intention of the figure.

“Additionally, while PDPN labels the cribriform plate lymphatic vasculature, it also defines the meningeal-immune interface at the border of both the olfactory bulb and olfactory nerve bundles.”

> *(2) While the PostContact-seq strategy is innovative (Figure 3), additional justification is needed to demonstrate that tissue dissociation did not artificially disrupt PDPN-myeloid contacts. The relatively small proportion of live PDPN-rich doublets (~2.5% total aggregates and ~18% PDPN+ within total aggregates) raises questions about representativeness compared with in situ observations. The authors should also more explicitly elaborate on why PostContact-seq was favored over alternative approaches such as PIC-seq.*

We acknowledge this important methodological concern. We have expanded the Methods section and added a dedicated paragraph in Results addressing the following:

Tissue dissociation controls: Dissociation protocols were used specifically to minimize cell-cell adhesion. Unfortunately, we cannot perform parallel dissociations of naive (non-EAE) cribriform plates for scRNAseq because PDPN^{+}-containing doublets are essentially non-existent. This is also supporting the representativeness compared to in situ observation. Doublets are significantly enriched in EAE tissue compared to naive controls, arguing against artifactual aggregate formation.

Representativeness of ~2.5% doublets: While the absolute proportion of doublets is modest, this is consistent with in situ observations where myeloid-PDPN contacts are spatially restricted to the outer perineural and meningeal niche rather than globally distributed. We argue this is simply the enrichment of a rare interaction rather than a limitation.

PostContact-seq vs. PIC-seq: “PIC-seq (Giladi et al., 2020) sequences intact doublets and relies on specialized deconvolution tools to parse apart data. PostContact-seq leverages the cellular contact signatures post-dissociation, making it a more accessible system. However, we now explicitly discuss this comparison in the Results and acknowledge PIC-seq as a complementary future approach in discussion.

> *(3) (Figure 4B): Clarification of integration across four methods; consideration of CellChat/NicheNet: The authors stated that results regarding cell-cell interactions were integrated across four intercellular communication methodologies (Figure 4B), but this integration is not clearly described in either the Results or Method sections. This needs clarification. Moreover, the interaction analysis in Figure 4B seems to rely on TALKIEN, which does not incorporate prior ligand-receptor knowledge. Given the availability of widely used tools, such as CellChat and NicheNet, the authors may consider cross-referencing their findings.*

We have revised the Methods sections to clearly describe our strategy for the TALKIEN analysis. Importantly, TALKIEN does integrate ligand receptor libraries from four sources: CellChat, CellPhoneDB, iCellNet, and the Ramilowsky datasets to generate its figures. Interactions reported in Figure 4B are those supported by this analysis, and we updated the text accordingly.

> *(4) Pseudotime trajectory analysis of CCR2^{+} monocyte differentiation.*
>
> *"A pseudotime trajectory analysis may be valuable to test whether CCR2^{+} monocytes preferentially differentiate into CHI3L3^{+} macrophages, PD-1^{+} DCs, or other subsets."*

We thank the reviewer for this insightful suggestion. We added a complete pseudotime analysis (Author response image 1). The pseudotime analysis tracks a continuous developmental trajectory starting from cDC2 and early macrophage populations (Pseudotime = 0, dark purple) and progressing through the main macrophage body toward an activated terminal state (Pseudotime = 16, yellow). Crucially, the trajectory correctly excludes non-continuous lineages such as resident microglia and lymphoid cells. This progression is functionally validated by the transient upregulation of the recruitment marker CCR2 during intermediate stages, which subsequently downregulates as cells transition into a mature phenotype.

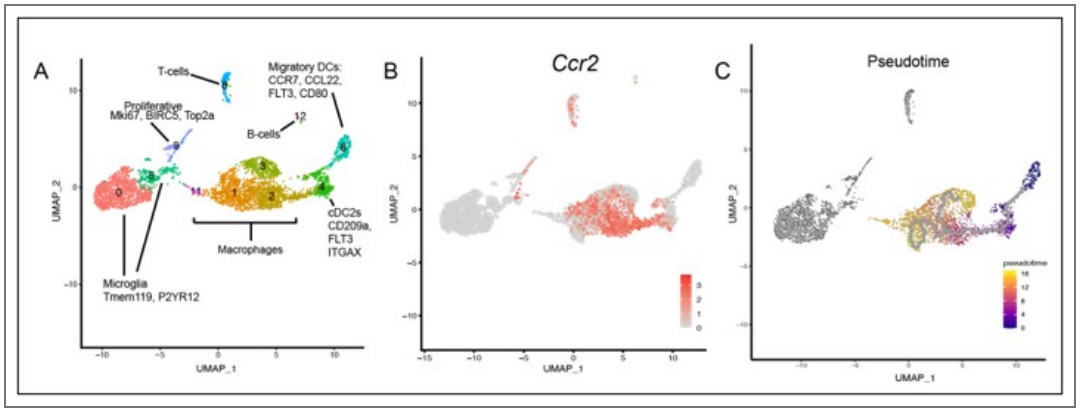

Author response image 1.

> *(5) FACS-based validation of macrophage immunosuppressive signatures.*
>
> *"Validation using the same post-contact vs. no-contact sorting strategy would strengthen the conclusions."*

This is an excellent suggestion and will be the topic of future detailed investigation focusing on the cellular and molecular reprograming of the immunosuppressive microenvironment at the cribriform plate.

> *(6) Identity of CD45IV$^+$ cells in contact with PDPN$^+$ cells (Figure 6B-C); gating strategy; tissue co-labeling. "Provide a gating strategy demonstrating that these are CD11b$^+$CD11c$^+$ DCs... whether dying cells are PD-1$^+$... co-labeling for PD-1, cleaved caspase-3, and CD11c-eYFP."*

A full gating strategy (now Figure S5) demonstrate sequential gating from Cells → Doublet → PDPN doublet → CD11b$^+$ CD11c $^+$ → CD45IV$^+$ (intravascular exclusion positive) within the doublet gate.

> *(7) (Figures 1F-H): Morphological differences of CD11c$^+$ cells.*

We have added commentary to the Results section noting that "CD11c$^+$ cells in the olfactory bulb parenchyma display a ramified, microglia-like morphology consistent with tissue-resident or parenchymal surveillance cells, whereas those infiltrating the cribriform plate perineural niche show a rounded, non-ramified morphology more consistent with recently recruited monocyte-derived DCs or macrophages." This morphological distinction aligns with our scRNAseq-defined population differences and supports the notion that the cribriform plate niche shapes distinct myeloid states.

> ***Reviewer #1 (Recommendations for the authors):***

> *(1) (Figure 1C): MHCII counts vs. MFI discrepancy*

Thank you for catching this. The text has been corrected to reflect that we counted number of cells in the PDPN+ region of the cribriform plate

> *(2) Proximity ligation assay (PLA) for macrophage-fibroblast ligand-receptor pairs*

We appreciate this suggestion. PLA validation of all predicted pairs is beyond the scope of this revision, and we are primarily interested in interactions occurring *in vivo* and *in situ*. Future studies will investigate properties of these cells using PLA.

> *(3) (Figure 2E vs 2G): Inconsistent quantification strategies; CSF1R-GFP/CD11c-eYFP validation of CHI3L3^{+}/Arg1^{+} cells*

Arg1 signal was more broadly expressed and it was hard to distinguish 1 cell vs 2 cells in close proximity. Which is why we elected to use %Arg1 in PDPN+ regions. Conversely CHI3L3 staining revealed more easily identifiable single cells for quantification. Nonetheless both methods achieve the purpose of outlining that these cells increase in number a the cribriform plate lymphatic regions.

> *(4) (Figure 3E): Pro-inflammatory features of migratory DCs vs. suppressive interpretation.*
>
> *"Pdcd1lg2, Cd80, Cd83 are associated with T-cell activation — how does this align with an immunosuppressive niche?"**

This is an excellent point that we now explicitly address in the Discussion. The co-expression of Pdcd1lg2 (PD-L2), Cd80, and Cd83 by migratory DCs likely reflects a tolerogenic activation state rather than a conventional immunostimulatory one. PD-L2 co-expression with costimulatory molecules has been documented in tolerogenic DCs that can engage T cells while simultaneously delivering inhibitory signals via the PD-1/PD-L2 axis (inhibiting rather than amplifying T-cell responses). Furthermore, the lower abundance of migratory DCs in post-contact samples relative to no-contact samples may reflect that cells expressing this immunological synapse machinery are preferentially undergoing programmed cell death (consistent with Figure 6 findings), leaving a post-contact population enriched for the macrophage-dominated tolerogenic signature. We now discuss this interpretation explicitly.

> *(5) (Figure 5F-G): Gating strategy for PD-1^{+} DCs — PDPN inclusion*

The gating strategy has been clarified in Figure S6 (new figure) and the Methods section. PD-1^{+} DCs shown in Figures 5F-G were gated from the PDPN^{+} doublet fraction specifically, paralleling the outlined scRNAseq approach. We have added PDPN as an explicit gate in the updated Figure S6A

> *(6) (Figure 5H): Discrepancy between text and data — "lowest genes" in PD-1neg DCs.*

We apologize for this error. The text has been corrected: the data in Figure 5H show that chemokines, ISGs, and MHC genes are among the highest expressed in PD-1^{+} DCs (not PD-1^{-}), consistent with the heatmap shown. This aligns with the interpretation that PD-1^{+} DCs, while tolerogenic, retain antigen-presentation and chemokine-signaling capacity.

> *(7) Figure 6 reference errors in Results text*

Corrected throughout — all references to cell death/apoptosis data now correctly cite Figure 6.

> ***Reviewer #2 (Public review):***

> *(1) Sorted populations — in vivo interactions vs. ex vivo aggregation artifacts*

As detailed in our response to Reviewer 1 (Weakness 2), due to the non-detectable doublet frequency in non-EAE mice, we believe that PDPN$^+$ doublet enrichment is EAE-dependent. We also used cold dissociation conditions. We also note that the transcriptional signatures recovered from PDPN$^+$ doublets are not simply a mix of independently sorted PDPN$^+$ and myeloid single-cell transcriptomes, they contain unique interaction-associated gene programs (e.g., elevated Pdcd1, tolerogenic markers) not present in non-contact controls, arguing for biologically meaningful contact rather than artifactual aggregation.

> *(2) PDPN as stromal vs. lymphatic endothelial cells — which is most relevant?*

We have clarified throughout the manuscript that PDPN in IHC marks at least two distinct populations at the cribriform plate: (1) PDPN$^+$LYVE-1$^+$ lymphatic endothelial cells and (2) PDPN$^+$LYVE-1$^-$ meningeal fibroblasts/perineural sheath cells. It is hard to dissociate which is most relevant in the present study.

> *(3) Descriptive nature; lack of functional correlates; implications need further discussion.*

We appreciate this honest assessment. We agree that functional experiments (e.g., conditional deletion of DC populations at the cribriform plate, blockade of PD-1/PD-L1 axis, lymphatic ablation) will be critical for establishing causality and are ongoing in the laboratory. In this revision, we have:

(1) Added a pseudotime analysis as a computational functional inference.

(2) Refined the Discussion to explore functional implications, including how tolerogenic conditioning at the cribriform plate may limit cervical lymph node priming, parallels with perineural immunosuppression in cancer, and therapeutic opportunities (e.g., modulating this niche to enhance or dampen CNS autoimmunity).

> ***Reviewer #2 (Recommendations for the authors):***
>
> *(1) (Figure 1E): What does PDPN thickness increase represent?*

We have added clarification to the Results and Discussion. Based on our data, the increased PDPN$^+$ layer thickness during EAE most likely reflects a combination of: (1) increased PDPN expression per cell (supported by elevated MFI in flow cytometry), (2) cellular hypertrophy of existing PDPN$^+$ cells. However we cannot fully discriminate between these mechanisms with the current data and acknowledge this as a limitation.

> *(2) (Figure 2A): In Figure 2A, can the authors provide a healthy control example to pair with 2A? Is the Chi3L3 expression "below" the plate...in the mucosa, associated with EAE, or the same in steady state? The images in 2D are hard to appreciate at the current size.*

Healthy (naive) control images are included in Figure 2D for direct comparison with EAE tissue, we added zoomed images of each panel to provide clearer context for the disease-associated changes in myeloid cell distribution and M2 marker expression.

> *(3) What is the denominator for the quantification in 2E? Is this per unit area? If so, is it the PDPN area or the total cribriform plate region area? If the area of PDPN increases (as the authors show), then the potential area that can hold YM1+ cells also increases, so the absolute number of cells comparison isn't that fair.*

We have added this distinction to the results.

> *(4) The same goes for 2G; however, in G, the quantification is "% Arg1+" ----percentage of what? The increase in Arg1 expression is striking, but it's also striking how similar the*

> *PDPN network appears between healthy and EAE in Figure 2F.*

We have added this distinction to the results And added a label of quantification to Figure 2G.

> *(5) Are these increases in Arg1+ cells occurring in the meninges of EAE mice? Or is this specific to perineural areas at the cribriform plate? In a sagittal plane, are these cells clustered tightly at the cribriform plate, or do they extend outward along the ON tracts?*

These are clustered tightly in the meningeal regions and along ON tracts. We do not have any sagittal sections available for further proper analysis.

> *(6) In Figure 2, some panels are labeled "merge" -what does this mean? The DAPI label within the figure is also impossible to see.*

Figure labels have been adjusted. Merge is a common label which identifies panels with all channels merged together in a series.

> *(7) Figure 3: The authors sort cells that interact with PDPN+ CD31+ double-positive cells before the scRNAseq analysis. However, it's not clear from these data that the PDPN expansion observed in their histochemistry is on stromal or endothelial cells. As the authors note, PDPN "also efficiently labels meningeal layers surrounding them along the olfactory nerve layer, including fibroblasts and their associated extracellular matrix (ECM)". Can the authors more clearly explain the rationale for using CD31 in this gating strategy?*

We sorted for CD11b+CD45+ (immune), CD31+ (endothelial), PDPN+ (meningeal fibroblasts). CD31 was used to isolate myeloid cells and endothelial cells at the brain's borders.

> *(8) Also, without having to do scRNAseq, could the authors compare the interacting populations for cells stuck with PDPN+CD31neg cells? Figure 3B indicates that a good number of these PDPN+CD31neg cells are present in the sort.*

We did not isolate PDPN+CD31- cells from our sort, in our experience these are mostly fibroblasts though. Future studies will look at cells which adhere specifically to PDPN+CD31- aggregates.

> *(9) The interacting cells seem to have a particular affinity for the sorted endothelial cells. However, it's not clear if these cells are simply seizing an opportunity to stick together once the cells are mechanically separated and spun down, or were together in vivo. The authors should determine how many of these cell types are maintaining an in vivo contact or simply are efficient at making new contacts ex vivo. One approach would be to take EAE tissues from CD45.1 and CD45.2 congenic animals and mechanically separate them together. Then the composition of doublets can be analyzed for the frequency of CD45.1/2 doublets or CD45.1 and CD45.2 single positive doublets....and also which cell types are contributing to these doublets. This will test how much of this interaction is driven by ex vivo stickiness or in vivo, and also give some idea about the inherent ability of these immune cells to find and engage PDPN cells.*

This is a limitation of the current study, and you have provided an excellent experiment and one we have added to discussion.

> *(10) Figure 4: I'm confused about Figure 4. If I'm reading this correctly, these are the same data from Figure 3 that were sorted for CD31 positivity. If that's the case, how are there fibroblasts in these data? Does this represent an aggregation of endothelial, fibroblast, AND immune? (CD31, PDPN, and CD11c).*

Yes we suspect that endothelial, fibroblast, AND immune aggregates are highly heterogeneous. Without negative sorting/gating we are left with high number of immune

cells in or sorting paradigm.

> *(11) The authors comment on the relatively unclear biological significance of PD1 expression by DCs (non-T cells) and note their previous report on PD1 ligand expression in this cribriform region. Do the authors detect differential PD1 ligand expression in this current study (singlet vs aggregate)?*

We have not detected any significant difference in CD274 expression between non-interactor and interactor populations.

> *(12) Are the FACS data Supplemental Figure 2 on singlet vs doublet DCs performed after Liberase treatment? The FACS plots for both doublet and singlet populations look very different in how they are rendered, with large cell numbers in the 10^-4 range for the doublet groups. Why is this?*

No liberase treatment was given in these experiments, we have updated the figure legend.

> *(13) It seems like the figure labeling has gone awry. On page 9, what should be Figure 5 is being called Figure 4...and further on, Figure 5 is being used for Figure 6 ("Blood derived" data)---this makes it pretty confusing.*

This has been corrected. Thank you.

> *(14) On page 10, the authors have written "Lowest genes in PD-1- DCs included chemokines CXCL9, CXCL10, IL-12b, interferon-stimulated genes (Ifit1, Ifit2 and Ifit3) and several MHC-related genes (H2-M2, H2-Eb2, H2-DMb2)". Is this correct? Based on my reading of the figure, "5H" is that not PD-1+ DCs instead of PD-1- DCs? Also, there is a typo, "Cxck10".*

Thank you for pointing this out. We have corrected.

> *(13) It's not clear what the statement "...these data support that Pdcd1 expression in migratory DCs exhibits an immunosuppressive gene signature..." means. The PD-1 marker cannot "exhibit" anything by itself. Is this intended to say that migratory DCs expressing PD1 exhibit an immunosuppressive phenotype?*

Yes this is a better way to say it, it has been corrected.

> *(14) Figure 6: These are really cool data about the influx of peripherally derived cells to the cribriform plate during EAE. However, it would be more meaningful to have other compartments to compare with. What is the IV+ percentage within the CNS or meninges more generally? And also, how do these CD11c+ CD11b+ aggregates differ in IV+ from "singlets"? The authors show that T cells are caught in the scRNA aggregates. Are these IV+? Can the authors provide additional discussion about the relevance of the Ghost+ data? What does this really mean? In Figure 6, Olfactory is misspelled 2x in A...and the "D" in CD45 is missing from B.*

Spelling mistakes have been corrected, thank you. Future investigations will compare IV+ recruitment and aggregations to dural and other brain regions. We suspect that some of the IV+ populations are T cells but our experiments do not allow for this distinction. We have added additional information regarding our interpretation of the Ghost+ data.

> *(15) The title of the paper indicates that a suppressive myeloid network is assembled, and certainly, there is gene and protein expression data that are consistent with the presence of "suppressive" cells. However, can the authors demonstrate that this "network" is performing a suppressive function in vivo?*

This is a great point. Our IHC is highly indicative of classical M2 phenotype accumulating at meningeal regions around the olfactory bulb. One experiment we are interested in is local ablation of macrophages at the CP, to determine their role in EAE disease progression.

> *(16) At the end of the discussion, the authors state, "They describe unique DC populations at the cribriform plate, one displaying pro-inflammatory and migratory features while the PDPN-associated population displayed more immunoregulatory characteristics". This seems a little bit misleading, or at least not giving the macrophages their due. A good part of the migratory DCs (as put in the figures) are associated with the Arg1+/Chi3l3+ macrophages. It's possible that suppression -if it's happening- could come from one or both cell types.*

We have removed that line and altered the discussion to more accurately reflect the results with respect to DCs and Macrophages.

> *(17) In this study, the authors focus on dendritic cell and macrophage populations in the context of autoimmune disease and chronic CNS inflammation. In a recent study, the authors show an important recruitment of immune cells in the cribriform plate during a CNS infection by Mycobacterium tuberculosis. Do Arg1+/Chil3l3+ macrophage and tolerogenic DC populations still exist in this context? It would significantly strengthen the field's understanding of how the cells of the cribriform behave in different conditions if you could describe whether these cells are context-specific or is it really specific to cribriform plate tissue?*

This is an excellent suggestion and will be the focus of future investigations.

We believe these revisions substantially strengthen the manuscript and directly address major concerns raised by both reviewers. We remain committed to the functional follow-up studies that both reviewers rightly identify as the natural next chapter of this work.

https://doi.org/10.7554/eLife.110460.2.sa0